SKIN INFLAMMATION

Classification of human chronic inflammatory skin disease based on single-cell immune profiling

Yale Liu[1,2,3]†, Hao Wang[4]†, Mark Taylor[2], Christopher Cook[2,3], Alejandra Martínez-Berdeja[2], Jeffrey P. North[2], Paymann Harirchian[2,3], Ashley A. Hailer[2,3], Zijun Zhao[5], Ruby Ghadially[2,3], Roberto R. Ricardo-Gonzalez[2,6], Roy C. Grekin[2], Theodora M. Mauro[2,3], Esther Kim[7], Jaehyuk Choi[8], Elizabeth Purdom[4]‡, Raymond J. Cho[2]*‡, Jeffrey B. Cheng[2,3]*‡

Inflammatory conditions represent the largest class of chronic skin disease, but the molecular dysregulation underlying many individual cases remains unclear. Single-cell RNA sequencing (scRNA-seq) has increased precision in dissecting the complex mixture of immune and stromal cell perturbations in inflammatory skin disease states. We single-cell–profiled CD45$^+$ immune cell transcriptomes from skin samples of 31 patients (7 atopic dermatitis, 8 psoriasis vulgaris, 2 lichen planus (LP), 1 bullous pemphigoid (BP), 6 clinical/histopathologically indeterminate rashes, and 7 healthy controls). Our data revealed active proliferative expansion of the T_{reg} and Trm components and universal T cell exhaustion in human rashes, with a relative attenuation of antigen-presenting cells. Skin-resident memory T cells showed the greatest transcriptional dysregulation in both atopic dermatitis and psoriasis, whereas atopic dermatitis also demonstrated recurrent abnormalities in ILC and CD8$^+$ cytotoxic lymphocytes. Transcript signatures differentiating these rash types included genes previously implicated in T helper cell (T_H2)/T_H17 diatheses, segregated in unbiased functional networks, and accurately identified disease class in untrained validation data sets. These gene signatures were able to classify clinicopathologically ambiguous rashes with diagnoses consistent with therapeutic response. Thus, we have defined major classes of human inflammatory skin disease at the molecular level and described a quantitative method to classify indeterminate instances of pathologic inflammation. To make this approach accessible to the scientific community, we created a proof-of-principle web interface (RashX), where scientists and clinicians can visualize their patient-level rash scRNA-seq–derived data in the context of our T_H2/T_H17 transcriptional framework.

INTRODUCTION

Atopic dermatitis (AD) and psoriasis vulgaris (PV), prototypical inflammatory skin diseases, collectively affect about 10% of adults in the United States (*1*–*3*). AD is classically viewed as a T helper 2 (T_H2)–skewed inflammatory disease, with PV displaying a T_H1/T_H17 predominance. Biologic therapies now successfully target specific, dysregulated immune pathways in each disease—interleukin-4 receptor subunit α (IL4Rα) or IL-13 inhibitors in AD and IL-17 or IL-23 antagonists in PV. Whereas these drugs represent marked advances in treatment, ~20 to 50% of patients still do not achieve substantial improvement on a given drug (*4*–*6*). One major challenge is the clinical heterogeneity of inflammatory skin disease (*7*), which can preclude a definitive diagnosis and complicates treatment choice. A molecular endotyping approach could offer clinicians more objective criteria to classify inflammatory disease and select therapy.

Identification of molecular abnormalities distinguishing inflammatory skin disease is challenging using bulk cell–based profiling methods, which likely obscure cell type–specific transcriptional dysregulation. Studies have attempted to overcome disease heterogeneity by comparing internally controlled patient populations (*8*). Single-cell RNA sequencing (scRNA-seq) has identified previously unknown disease-specific perturbations across diverse inflammatory pathologies (*9*–*13*). Such high-resolution methods capturing simultaneous molecular portraits of different cell types are particularly appealing in human skin, where the complex composition of tissue limits mechanistic biology. scRNA-seq studies of AD-affected skin reveal increased type 2/type 22 T cells, inflammatory dendritic cells, and tissue-resident memory T (Trm) cells (*12*, *14*, *15*). Dupilumab-treated AD is characterized by persistence of transcriptionally defined mature dendritic cell subsets and Trm subpopulations (i.e., type 2/type 22 T cells and T_H2A) (*11*). In PV, single-cell transcriptomic studies show increased T_H17/Tc17 cells in active lesions, with two nonexhausted, *CXCL13*-expressing Tc17 subpopulations correlating with disease severity (*9*, *12*). However, these advances do not clarify whether inflammatory skin diseases as a whole can be reliably molecularly classified on the patient level.

In this study, we hypothesized that by focusing exclusively on cutaneous immune cells and applying increased analytic resolution (i.e. 41 cutaneous immune cell type classes), scRNA-seq approaches could improve identification and understanding of molecular abnormalities discriminating AD and PV. T cells and antigen-presenting cells (APCs) from rashes were profiled using unbiased single-cell droplet microfluidics RNA (10X Genomics) (*16*) and protein epitope [cellular indexing of transcriptomes and epitopes by sequencing (CITE-seq)] (*17*) approaches. Our study targeted a series of eight PV,

[1]Department of Dermatology, The Second Affiliated Hospital of Xi'an Jiaotong University, Xi'an, ShaanXi 710004, P. R. China. [2]Department of Dermatology, University of California, San Francisco, San Francisco, CA 94107, USA. [3]Dermatology, Veterans Affairs Medical Center, San Francisco, CA 94121, USA. [4]Department of Statistics, University of California, Berkeley, Berkeley, CA 94720, USA. [5]Santa Clara Valley Medical Center, Santa Clara, CA 95128, USA. [6]Department of Immunology and Microbiology, University of California, San Francisco, San Francisco, CA 94143, USA. [7]Department of Plastic Surgery, University of California, San Francisco, San Francisco, CA 94107, USA. [8]Department of Dermatology, Northwestern School of Medicine, Chicago, IL 60611, USA.
*Corresponding author. Email: raymond.cho@ucsf.edu (R.J.C.); jeffrey.cheng@ucsf.edu (J.B.C.)
†These authors contributed equally to this work.
‡These authors contributed equally to this work.

seven AD, and also six clinical/histopathologically indeterminate rashes (CIRs), which presented in adulthood and harbored clinical and histopathologic features of both PV and AD. To more precisely define the cell type–specific transcriptional alterations distinguishing these diseases, we used molecular signatures to investigate and segregate these CIRs in the context of AD and PV. We also created a web-based interface to help clinicians and scientists classify their clinically indeterminate skin rash cases.

RESULTS

scRNA-seq detected conserved skin CD45$^+$ immune cell classes

Our dataset included eight samples of PV, seven samples of AD, one case of BP, two cases of LP, six CIRs harboring clinical and histopathologic features of both PV and AD, and seven healthy controls (HCs). Additional clinical characteristics for each sample are described in table S1. After enzymatic digestion of donor skin biopsies, we flow-sorted live CD45$^+$ cells and performed Chromium 3′ scRNA-seq and CITE-seq protein epitope sequencing. We obtained transcriptomic data from 158,037 single cells after quality control filtering (removal of doublets and poor-quality cells). Using Seurat, clustering was performed using Louvain community detection–based modularity optimization (*18*). We first used a resolution parameter of 0.4 based on clustree optimization approaches (*19*), delineating 16 immune cell clusters, including 6 lymphocyte clusters (*CD3*$^+$ or *KLRB1*$^+$), 9 APC clusters [human leukocyte antigen (*HLA*)–*DRA*$^+$], and a mast cell cluster highly expressing *TPSAB1* (tryptase) (fig. S1, A and B, and table S2).

We speculated that more finely demarcating immune cell populations might reveal new cell type–specific expression differences, either between healthy and inflamed skin or between disease classes. We separately subclustered the *CD3*$^+$/*KLRB1*$^+$ lymphocyte populations and *HLA-DRA*$^+$ APC populations into 23 and 24 higher-resolution classes, respectively, again based on clustree-based optimization. After removal of clusters containing mostly nonimmune or low-quality cells, 21 *CD3*$^+$/*KLRB1*$^+$ clusters and 19 *HLA-DR*$^+$ clusters were retained (fig. S1C). Including the previously described mast cell cluster, this classification generated 41 final clusters [displayed as a Uniform Manifold Approximation and Projection (UMAP) representation

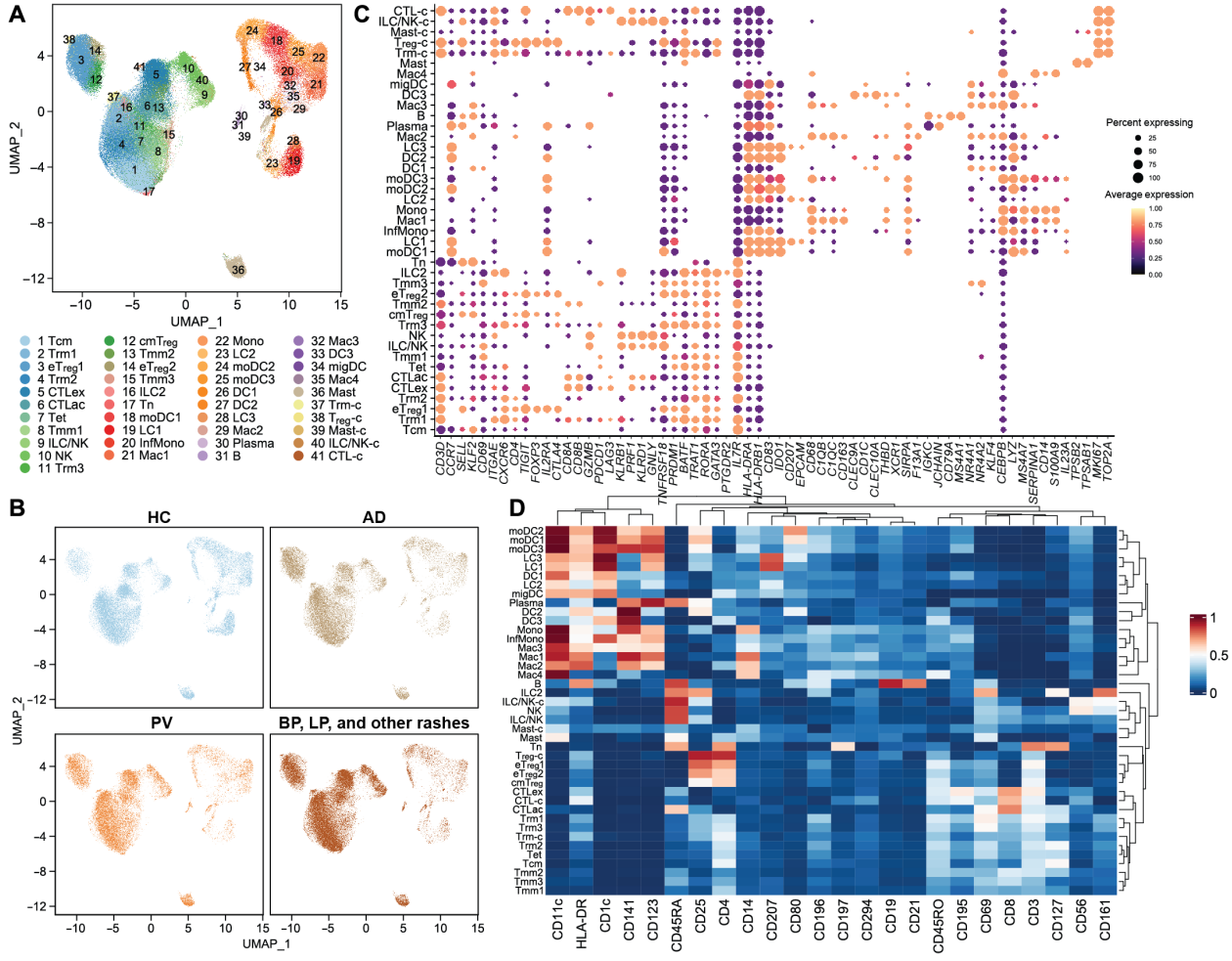

Fig. 1. Immune single-cell landscape of rash-affected and healthy control human skin (31 samples). (**A**) UMAP representation of 41 scRNA-seq defined immune cell classes. (**B**) UMAP representation of cell distribution across immune cell classes for disease classes and HC skin. (**C**) Expression of critical marker transcripts (columns) distinguishing immune cell classes (rows). Size of dots represents the fraction of cells expressing a particular marker, and color intensity indicates mean-normalized scaled expression levels. (**D**) Expression of protein epitope (CITE-seq) markers for the 41 transcript-based immune cell clusters. Color intensity represents fraction of cells expressing a given marker.

in Fig. 1A and tables S3 and S4]. Larger immune clusters were well represented across healthy control and major disease classes, suggesting limited distortion from sample-specific batch effects (Fig. 1B and fig. S1D).

We next assigned identities to the 41 immune cell populations by comparing marker genes for each cluster (i.e., the most differentially expressed transcripts or epitope markers between cells in that cluster versus all other cells; table S5) against canonical markers for established cell types. Among T cells, we identified two *CCR7*$^+$, *SELL*$^+$, *KLF2*$^+$ (*20*), *CD3D*$^+$ populations, one corresponding to central memory cells (Tcm) with elevated CD69 and CD45RO protein epitope expression (CITE-seq data) and one smaller cluster representing a naïve T cell population with high CD45RA protein expression (Fig. 1, C and D). We also identified three *CCR7*$^+$/*SELL*$^-$ migratory memory classes (Tmm1, Tmm2, and Tmm3) (*21*). Three *CD3D*$^+$ T cell clusters expressed Trm cell marker transcripts *ITGAE* (*CD103*), *CXCR6*, and the CD69 protein epitope (CITE-seq data) (*22*), which we termed Trm1, Trm2, and Trm3 and contained both *CD4*$^+$ and *CD8A*$^+$ cells (Fig. 1, C and D). Three other *CD4*$^+$ populations were identified as regulatory T (T_{reg}) cells based on the expression of *FOXP3*, *TIGIT*, *CTLA4*, *IL2RA* (*CD25*), and *IKZF2* (*Helios*) (Fig. 1C) (*23*, *24*). Two of these T_{reg} cell populations displayed effector markers (*TNFRSF18* and *PRDM1*) (*25*) and were termed $eT_{reg}1$ and $eT_{reg}2$, whereas a third CD45RO$^+$ class harboring *SELL* and *CCR7* transcript was classified as central memory T_{regs} (cmT_{reg}; Fig. 1, C and D) (*26*). A small *CD3D*$^+$ T cell cluster bearing elevated levels of numerous epigenetic regulators, transcription factors, and long noncoding RNAs—such as *BATF*, *SNHG12*, and *ZFAS1*—was named Tet.

Two *CD8A*$^+$*CD8B*$^+$ clusters were defined as cytotoxic T lymphocytes based on expression of *GZMB*, *NKG7*, and *CCL5*, including an activated cluster (CTLac) expressing *TNFRSF4*, *TNFRSF18*, and *CD96* (*27*, *28*), and a closely related class enriched in canonical exhaustion markers such as *PDCD1* and *LAG3* (CTLex) (Fig. 1C) (*29*). We also defined three innate lymphoid/natural killer cell populations as *KLRB1* (*CD161*)$^+$ with absent or relatively low *CD3D*, *CD19*/*MS4A1*, *CD14*, and *HLA-DRA* expression (*30*). Of these, one small cluster expressed the type 2 transcriptional factors *GATA3* and *PTGDR2* and was identified as an innate lymphoid cell population (ILC2) (*12*). Two populations of *KLRD1*$^+$, *GNLY*$^+$, *PRF1*$^+$, and *GZMB*$^+$ cells were assigned as either natural killer (NK) or ILC/NK cells, with the former expressing high levels of the CD56 epitope by CITE-seq (Fig. 1, C and D).

We also identified a group of myeloid lineage subpopulations (*31*) (Fig. 1, C and D). Four macrophage populations were enriched for *CD68*, *CEBPB,* and *FCER1G* (*32*). Two were distinguished by complement transcripts *C1QB* and *C1QC* as well as the scavenger receptor *CD163* (Mac1 and Mac3), another by alternative activation and suppression markers *NR4A1*, *NR4A2*, *KLF4* (Mac2) (*12*), and the fourth by monocyte (Mono) markers *CD14* and *S100A9* (Mac4). Three Langerhans cell populations (LC1, LC2, and LC3) were identified on the basis of *CD207* transcript and protein and *CD1c* and *EPCAM* expression.

Five Mono or Mono-derived cell populations shared expression of Mono-associated genes *MS4A7*, *LYZ*, and *SERPINA1* (Fig. 1C) (*33*). One cluster representing classical Monos expressed higher levels of *CD14* transcript and protein and *S100A9* (Fig 1, C and D) (*34*), whereas we designated another inflammatory Monos (InfMono) because of enrichment for *IL1B*, *IL23A*, and *CXCL3* (*12*). The three remaining clusters also expressed major histocompatibility complex II molecules (*HLA-DRA* and *HLA-DRB1*) and were labeled Mono-derived dendritic cells (DCs) (moDC1, moDC2, and moDC3). We identified four DC classes (*HLA-DRA*$^+$), one enriched in *CD1C* and *CLEC10A* (DC1), with two others expressing *CLEC9A*, *CLEC10A*, and *XCR1* (DC2 and DC3) (Fig. 1C) (*12*). There was an additional migratory DC population that expressed *CD1C* and migratory/mature markers, such as *FSCN1*, *LAMP3*, and *CCR7* (*35*).

Two minor populations were enriched in immunoglobulin (Ig) genes (*IGHG*, *IGHA*, *IGKC*, and *JCHAIN*), consistent with B cell lineage. One was identified as B cells (*CD19*$^+$ and *MS4A2*$^+$; Fig. 1C), also enriched for CD19 and CD21 epitopes (Fig. 1D), and one as plasma cells (*CD19*$^-$, *MS4A2*$^-$, and *IGHG1*/*IGHG4*$^+$) (*36*). A large population of mast cells (Mast) was easily distinguished by expression of *TPSAB1* (tryptase) and *TPSB2* (Fig. 1C) (*37*).

Five clusters showed elevated cell division transcripts, such as *MKI67*, *TOP2A*, *CENPF*, and *UBE2C* (Fig. 1C) (*38*). Four of these cycling cell subpopulations mapped closely to existing T cell clusters and were named accordingly: T_{regs} (T_{reg}-c), Trm (Trm-c), CD8$^+$ cytotoxic T cells (CTL-c), and NK and ILC cells (NK/ILC-c). One mitotically active myeloid group expressed mast cell markers and was named Mast-c.

We clustered our CD45$^+$ cells into a comparatively large number of classes to maximize discovery of molecular abnormalities that might be obscured in conflated populations. Our classification comported well with both other published scRNA-seq cutaneous immune cell landscapes (fig. S1, E and F) (*11*, *12*) and canonical CD45$^+$ classes. As the latter classifications were developed primarily from flow cytometry experiments in blood and other noncutaneous tissues, we expected our approaches to yield some small differences in subclass definition. Overall, our scRNA-seq–derived analysis retrieved most well-established skin CD45$^+$ immune cell populations, with robust representation in both rashes and HCs.

Inflamed skin is characterized by CD8$^+$ T cell exhaustion and T_{reg} expansion

To discern differences in immune cell composition between healthy control and rash-affected skin, we first calculated each cluster's aggregate representation in each of these two states. This analysis showed that inflammation was accompanied by relative increases in multiple lymphoid cell classes and proportionate decreases in myeloid populations (Fig. 2A). We next applied a weighted Gaussian linear model to compare healthy control and rash-derived CD45$^+$ cell proportions (see the "Weighted Gaussian linear model for differential immune cell composition analysis" section in Materials and Methods), identifying 27 clusters with statistically significant alterations (Fig. 2B). Chronic inflammatory skin diseases showed an increase in exhausted CD8$^+$ T cells (CTLex class up 80.4%, from 4.5 to 8.2%), highlighting marked exhaustion of CD8$^+$ cells in virtually every rash sample assayed (table S6). We also noted a substantial expansion of all three T_{reg} classes (2.19- to 3.13-fold), generalizing a trend reported anecdotally in some rash types (table S6) (*39*). Resident memory T cell classes were also proportionately increased, with Trm1 up 71.4% from 6.3 to 10.7% and Trm2 up 108.7% from 4.3 to 9.0%, (table S6). Mitotically active cell clusters were markedly expanded in rashes, revealing active proliferation of Trm, T_{reg}, ILC/NK, and CD8$^+$ T cell populations in lesional skin (Fig. 2B and table S6).

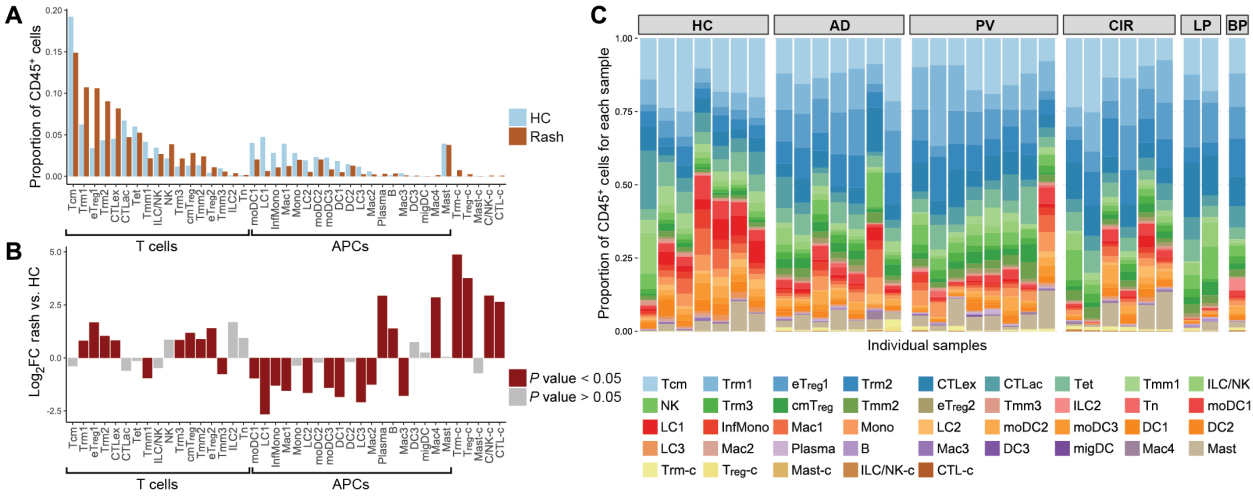

Fig. 2. Enrichment of T_{reg}, Trm, and exhausted CD8$^+$T cell populations in rash-affected skin. (**A**) Distribution of immune cell populations for 7 HC and 24 rash-affected (Rash) skin samples. *X* axis represents different immune cell populations. *Y* axis represents proportion of CD45$^+$ immune cells for each immune cell population in either rash-affected or HC skin. (**B**) Quasi-binomial model $\log_2$ fold change for rash-affected versus HC skin (*y* axis); unpaired two sample t test was used. *X* axis represents different immune cell populations. Red colored bars indicate statistically significant changes (*P* value < 0.05). (**C**) Proportion of CD45$^+$ immune cell subpopulations for each individual sample.

Analyses specific to AD and PV were also performed. Cell population frequency assessment for PV and AD showed similar patterns for CTLac, Trm1, and Trm2 cell populations (in AD, down by 34.9, up by 70.2, and up by 109.6%, respectively; in PV, down by 29.2, up by 84.5, and up by 89.1%, respectively; fig. S3 and table S6). However, CTLex and NK cells were more elevated in PV than in AD (in PV versus HC samples, up by 74.6 and 99.4%, respectively; in AD, up by 23.0 and 20.4%, respectively; fig. S3 and table S6). Although absolute cell numbers were low, plasma and B cells also both showed significant increases in rash samples in aggregate and for plasma cells in both AD and PV (relative to HC skin; table S6). Both disease-level analyses again showed expanded T_{reg} and Trm cells and exhausted CD8$^+$ T cells, suggesting involvement of these subpopulations in initiating or maintaining cutaneous inflammation.

Distinct, cell type–specific patterning differentiates forms of pathologic skin inflammation

We applied a hurdle model–based analysis of single-cell transcriptomics (MAST) (*40*) across all 41 CD45$^+$ cell populations to detect differentially expressed genes (DEGs) between (i) lesional PV and HC skin, (ii) lesional AD and HC skin, and (iii) lesional AD and PV skin (table S7). In each comparison, we required an absolute $\log_2$ fold-change difference of 0.425 and $P < 0.001$ of genes for further consideration.

The Trm1, CTLac, ILC/NK, Trm3, moDC1, InfMono, Mono, and LC2 populations showed abundant DEGs differentiating inflamed versus control skin (Fig. 3A and table S11). For example, the number of DEGs for PV versus HC and AD versus HC comparisons in Trm1 were 531 and 327, respectively; in CTLac, 306 and 574; and in InfMono, 522 and 451 (Fig. 3A and table S11). In distinguishing AD from PV, these eight T cell and APC populations also displayed the most statistically significant DEGs (Fig. 3A). For example, DEGs that differentiated AD and PV numbered 95 in Trm1, 137 in CTLac, and 242 in InfMono (Fig. 3A and table S11).

The treatment of single cells as distinct data sources in DEG approaches such as MAST generates very low *P* values for even relatively small fold-change differences. We reasoned that such small differences were more likely to be biologically meaningful if observed in multiple samples. We therefore applied a stringent filter in which at least 80% of individual AD or PV samples were required to display statistically significant differential expression for a given DEG, in comparison to all HC samples. The largest number of statistically significant DEGs passing this heterogeneity filter generally resided in the clusters containing the most cells, likely because of the increased effective sample size in these comparisons. However, Trm1 had a disproportionately large number of DEGs in the three comparisons (e.g., in the PV versus HC comparison, 514 DEGs for Trm1 cells compared to 197 for Tcm and 238 for $eT_{reg}1$ cells; Fig. 3B and table S11).

We next examined PV versus AD transcriptional abnormalities that met the aforementioned criteria for at least one lymphocyte population. We reasoned that DEGs identified in this way would be dysregulated in most of our patient samples but exclude nonspecific inflammatory genes present in both diseases. We observed that such PV-specific up-regulated genes were heavily concentrated in skin-resident memory classes Trm1 and Trm3, although there was also marked involvement of all migratory memory classes (Fig. 3C). An abundance of T_H17-linked transcripts was immediately apparent. In addition to the known PV markers *IL17F* and *CXCL13* (*9*), these PV-specific up-regulated DEGs include granulysin *GNLY* and *CTLA4*, whose loci have been linked genetically to PV (*41*, *42*), *KLRB1*, which is down-regulated by the tumor necrosis factor–α blocker alefacept in psoriatic lesions (*43*), *MGAT4*, which is down-regulated during ustekinumab treatment of psoriatic arthritis (*44*), and *PIK3R1* whose germline loss of function impairs cutaneous immunity (*45*). We also detected recurrent overexpression of signaling components such as *MAP3K4* and *PTPN13* restricted to the Trm1 and Trm3 classes, possibly helping explain why such

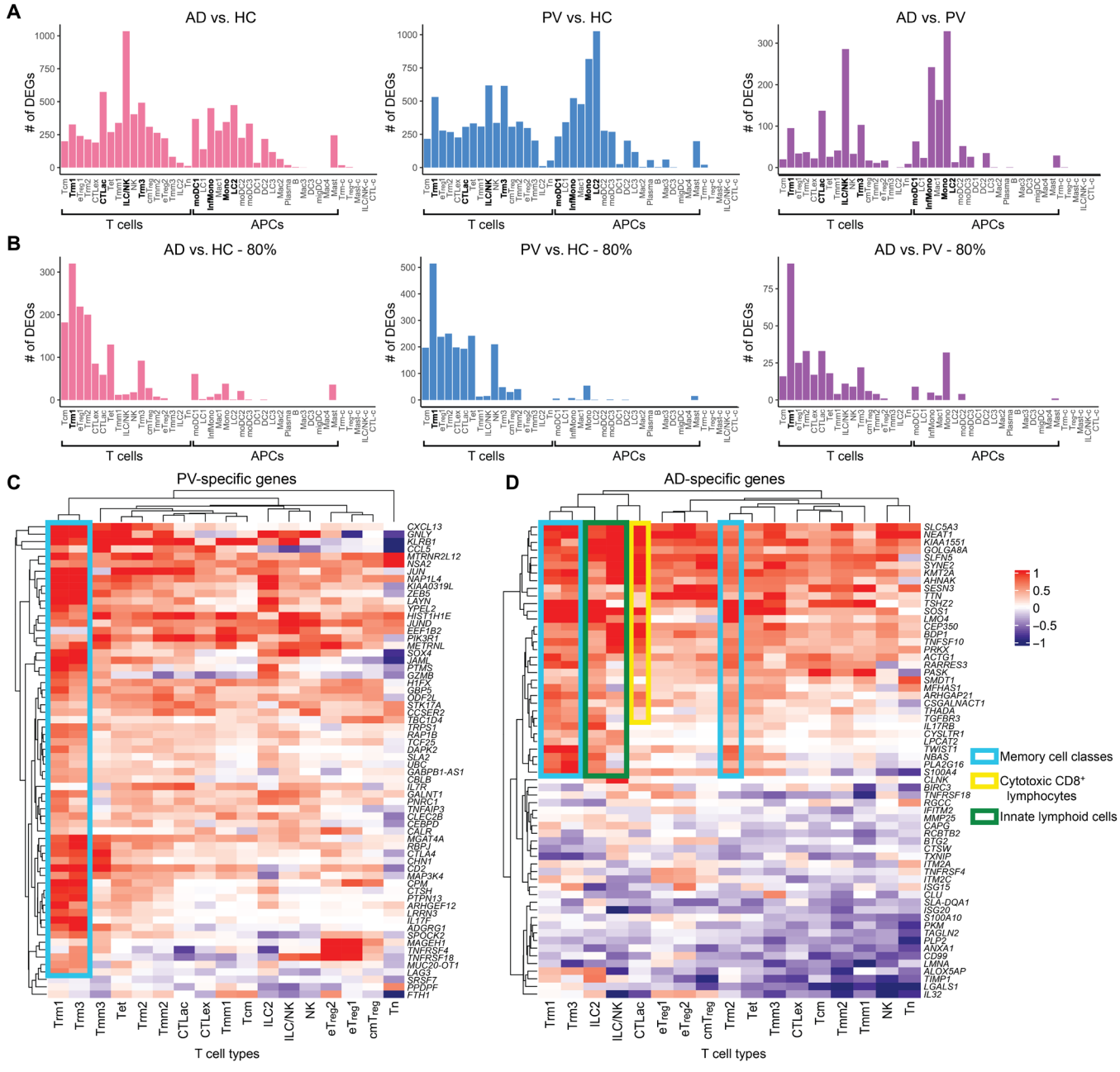

Fig. 3. Conservatively selected transcriptional abnormalities discriminating PV and AD demonstrate cell type–specific patterning. (**A**) Number of DEGs per immune cell population for AD and PV based on the MAST statistical framework. Number of DEGs (adjusted *P* value < 0.001, absolute $\log_2$FC > 0.425; on *y* axis) for each immune cell population (*x* axis) for seven AD versus seven HC sample comparisons (left), eight PV versus seven HC samples (middle), and seven AD versus eight PV samples (right). (**B**) Number of DEGs per immune cell population for AD and PV comparisons as in (A) but for DEGs present in 80% of samples from a disease class. (**C** and **D**) Heatmap showing immune cell population–specific transcriptional patterns for PV-specific genes (C) and AD-specific genes (D) (table S7) across lymphocyte subtypes (columns). Color key reflects the average $\log_2$FC for eight PV versus seven HC samples (C) or seven AD versus seven HC samples (D).

disease-specific transcripts have not been reported in prior bulk analysis studies (table S7).

Skin-resident memory classes also prominently expressed AD-specific up-regulated DEGs (Fig. 3D), including the known T_H1-inhibiting transcriptional regulator *TWIST1* (*46*), *IL17RB*, which has been implicated in the related T_H2 diathesis of asthma (*47*), and the candidate AD susceptibility loci *NBAS* and *CYSLTR1* (*48*, *49*). A similar number of AD-specific transcripts were also elevated in ILC classes and effector memory CTLs, including *MLL1* (*KMT2A*), an epigenetic regulator required to maintain T_H2 memory cell responses (*50*), the lncRNA *NEAT1*, which up-regulates T_H2 cytokines in $CD4^+$ T cells, and the experimentally T_H2-inducible transcript *AHNAK* (*51*). This pattern reinforced existing models positing a central role for ILC

(*52*) and $CD8^+$ T cells (*53*, *54*) in the pathogenesis of atopic diatheses (table S7).

For both PV and AD, fewer DEGs were detected in regulatory T and exhausted $CD8^+$ T cells (Fig. 3, A and B, and table S11). Differentiating transcripts were also sparse in APC classes, which frequently contained less than 100 cells per sample, underpowering them for DEG discovery (Fig. 3, A and B, and table S11). However, we did detect elevated expression of the antimicrobial gene epiregulin in atopic patients, consistent with its previous discovery in nonlesional skin from atopics (*55*), in both classical Monos and the macrophage class Mac1. Atopic Monos also harbored elevated transcripts of the inflammatory protein *S100A4*, previously identified as a pro-T_H2 mediator (*56*), and *AREG* was highly expressed in mast cells from psoriatic skin, potentially contributing to psoriasiform epidermal hyperplasia (table S7) (*57*). Similar DEGs were observed when differential expression analyses were reperformed using an alternative, nonparametric (Mann-Whitney) approach (fig. S4).

Skin-resident memory T cell DEGs distinguish PV versus AD samples in a validation cohort

To further assess disease specificity of these transcripts, we focused on lymphocyte subpopulations, in which the most DEGs were found. We generated gene set average expression scores for these DEGs that met the stringent criteria as an AD- or PV-specific gene in at least 80% of samples for at least one lymphocyte subpopulation (table S7 and the "Differential expression analysis between rash-affected and HC skin" section in Materials and Methods). As in the Fig. 3 (C and D) heatmaps, we saw that AD-specific gene expression was accentuated in skin-resident memory T cells, ILC classes, and effector memory CTLs of AD samples, whereas PV-specific genes were most prominently represented in skin-resident memory T cells of PV samples (Fig. 4, A and B).

We examined the Trm1 cell class because it harbored the largest number of conserved PV- and AD-specific DEGs (Fig. 3) and is functionally implicated in both diseases (*58*, *59*). As the Trm1 population likely contained closely interrelated cell types [e.g., Tc17 cells express Trm protein epitopes; (*60*)], we manually gated for Tc2/T_H2 cells, Tc17, and T_H17 cells to better understand cell subtypes within this cluster. In PV samples, there was a large proportional increase of Tc17 and T_H17 cells, whereas in AD samples, there were more Tc2/T_H2 cells, consistent with previous studies (fig. S5) (*12*). For Trm1 cells, the CD4:CD8 cell ratios in AD and PV samples were roughly comparable (fig. S6).

Whereas the relative proportions of these Trm1 cell subtypes alone could not discriminate AD from PV samples, we reasoned that DEGs from this population might. We thus tested the discriminative power of Trm1 AD- and PV-specific genes in an unrelated, external dataset (three PV and four AD samples from Reynolds *et al.* (*12*)). First, we calculated gene set expression scores for our Trm1 AD- or PV-specific genes in a transcriptionally analogous Trm population from the Reynolds *et al.* dataset samples (Fig. 4C, table S7, and the "Differential expression analysis between rash-affected and HC skin" section in Materials and Methods). We also used these AD- and PV- specific Trm1 DEGs to visually map relatedness of these external dataset samples (Fig. 4D and the "Hyperdimensionality proximity analysis" section in Materials and Methods). By both measures, our disease-specific DEGs accurately identified the two rash types in the Reynolds *et al.* dataset (Fig. 4, C and D). Thus, we demonstrated the potential to identify rash type, on a patient level, based entirely on molecular data from Trm1 cells.

Transcriptional abnormalities differentiating PV and AD in skin-resident memory cells segregate within unbiased functional networks

We sought to assess the functional significance of the hundreds of DEGs identified by our scRNA-seq approach. We again focused on the Trm1 cluster, which contained the established PV genes *IL17F*, *IFNG*, and *CXCL13* (*9*). We mapped PV- and AD-specific Trm1 DEGs (table S7) onto a coexpression correlation network built on our scRNA-seq data. Gene-gene transcriptional correlation values were calculated and the resulting network visualized by qgraph (*61*). The AD- and PV-specific genes segregated sharply in this network (Fig. 5A), which was expected because such differences in single-cell expression aided in their discovery. We next evaluated the functional interrelatedness of these PV- and AD-specific genes. We looked for interactions among these DEGs using an external database of known and predicted protein-protein interactions (STRING) and identified 98 protein nodes (genes), which formed 394 interactions (Fig. 5B) (*62*). As visually apparent, the PV- and AD-associated genes occupied distinct sectors of the protein-protein functional interaction network, recapitulating their segregation in the transcriptional expression network (Fig. 5A). We quantified this functional segregation by calculating the normalized cut score (*63*) between AD- and PV-specific genes, which compares the weighted number of edges connecting two groups relative to those within each group. These two groups showed significantly smaller linkages between the two groups than in multiple permutation tests that randomly assigned these genes to the AD- and PV-specific categories ($P = 0.001$; Fig. 5B). The segregation of PV- and AD-specific Trm1 genes in both transcriptional and protein interaction networks further supports a model in which coherent pathways drive these two disease classes.

CIRs, BP, and LP share molecular features with AD or PV

Many adult-onset rashes do not completely match clinical and histopathologic criteria for classic AD or PV, causing diagnostic and therapeutic ambiguity. Instead, these clinically indeterminate cases harbor overlapping eczematous/spongiotic features (as typically seen in AD) and psoriasiform patterns, either by histopathology or clinical presentation (*64*). We termed such cases CIRs. Six CIRs were profiled by scRNA-seq in this study whose clinical features were summarized in table S1. These patients lacked a clinical history consistent with canonical AD, i.e., eczematous rashes or lichenification in flexural areas beginning in early childhood. All patients with CIR were offered a trial on the IL4Rα-blocking AD treatment dupilumab, three of whom accepted. Two of the patients (CIR-A and CIR-B) showed near resolution of itch and clinically appreciable lesions within 2 months of treatment initiation. The third patient, CIR-E, suffered from a dermatitis with some eczematous features, including a spongiotic histopathology, in a background of known PV. This patient's rash showed no improvement after 3 months of dupilumab treatment.

We used our PV- and AD-distinguishing DEGs from the Trm1 population from Fig. 5 to group these samples (table S7). CIR-A and CIR-B, the dupilumab–responsive cases, segregated more closely with AD (Fig. 6, A and B). The lone dupilumab failure, CIR-E,

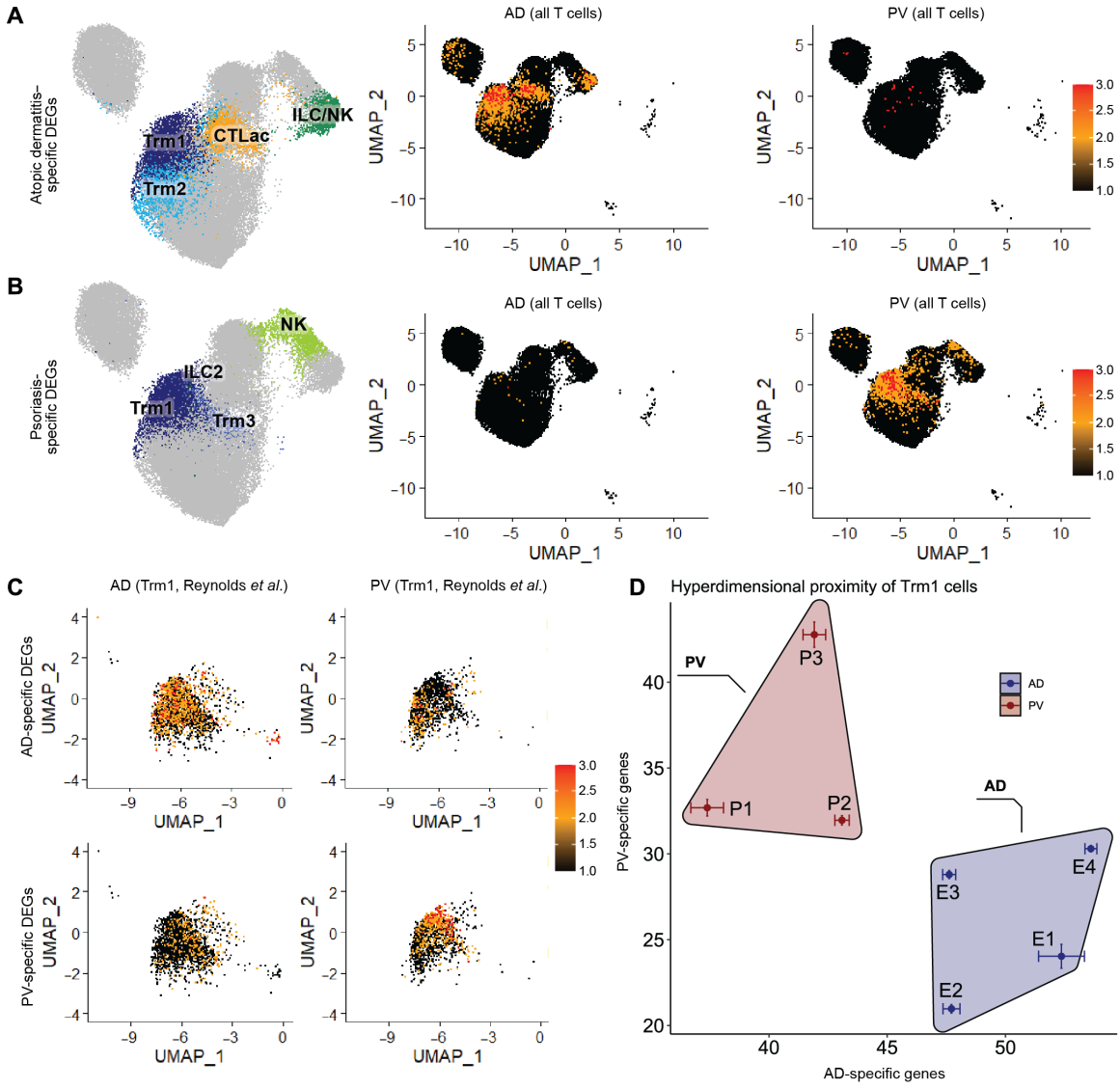

Fig. 4. AD and PV-specific gene module scores are elevated for their respective disease classes and classify samples from an external dataset. (**A** and **B**) Cell populations that corresponded to high-scoring AD and PV gene set scores. (A) AD- and (B) PV-specific lymphocyte DEG set (table S7) expression scores (calculated by Seurat AddModuleScore) displayed for lymphocytes on a single-cell level from seven AD samples (middle) and eight PV samples (right) in pseudocolored feature plots. (**C**) AD- and PV-specific Trm1 DEG set (table S7) scores displayed on a single-cell level for Trm1 cells in pseudocolored feature plots for four AD (left) or three PV (right) samples from the Reynolds *et al*. dataset (*12*). (**D**) Hyperdimensionality plot classification of the Reynolds *et al.* AD and PV validation cohort using AD- and PV-specific Trm1 DEG set modules from this study (table S7).

segregated with PV. To develop a test of significance, we calculated all-versus-all distances in the hyperdimensional plane for AD- and PV-specific genes in Trm1 cells and then asked whether the proximity of any CIR profile was closer to the PV centroid or the AD centroid than expected by random chance. The statistically derived distances show that samples CIR-A, CIR-B, and CIR-C are significantly more similar to AD, whereas CIR-E and CIR-F are more similar to PV (Fig. 6C and table S8). The histopathology of the CIRs that molecularly stratified with AD did not more closely resemble AD, nor did the histology of the CIRs that molecularly stratified with PV more closely resemble PV. As we were unable to classify CIRs merely by the presence of the previously described Tc2/T_H2 and Tc17 subpopulations within the Trm1 cluster, these observations reinforced the potential value in molecularly classification using disease-specific gene sets. We also tested how our PV- and AD-distinguishing DEGs would classify our two LP and one BP samples. In both the heatmap representations and hyperdimensionality map (fig. S7 and table S8), we saw the BP sample segregate more closely with AD and the LP samples with PV.

A web interface (RashX) to visualize patient-level rash scRNA-seq–derived data in context of this T_H2/T_H17 sample framework

Atypical rashes that are not easily classified into canonical clinical categories, such as the CIRs, occur frequently in dermatology clinics. We constructed a proof-of-principle interface, RashX (hosted at

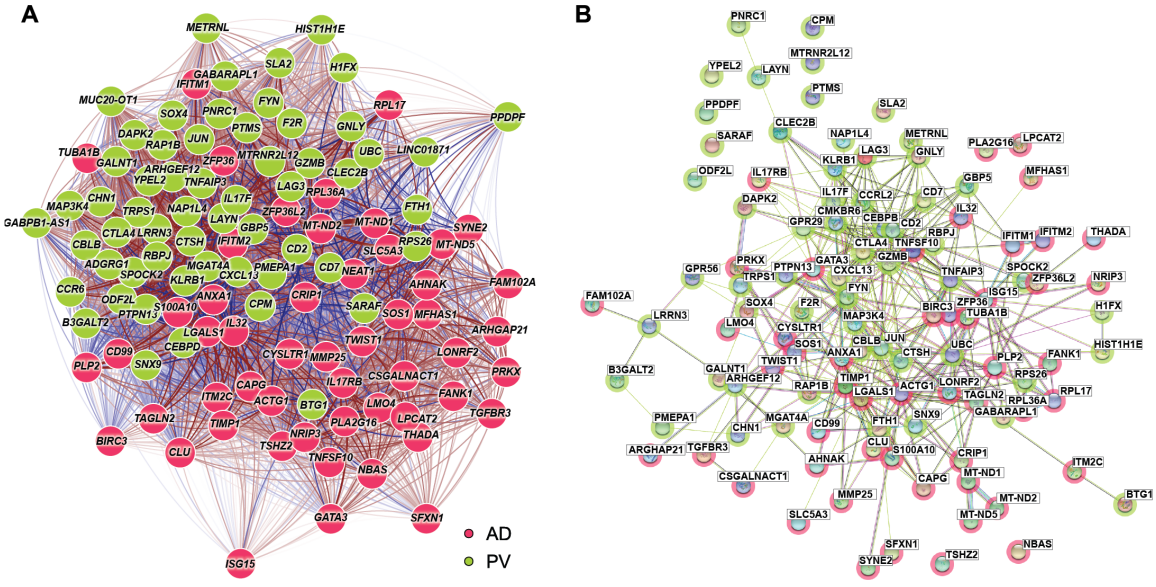

Fig. 5. AD and PV-specific DEGs segregate discretely on the basis of unbiased pathway and network analysis. (**A**) Transcriptional network (qgraph) for Trm1 AD- and PV- specific genes (table S7). The Fruchterman-Reingold algorithm was used to determine the network layout. Color shading of the gene nodes denotes AD (green)– or PV (red)–up-regulated genes. Red lines represent positive correlation, whereas blue lines represent negative correlation. Edges and links are shown for the correlation values from scRNA-seq data, with stronger edge intensity or thicker links signifying correlation. (**B**) STRING protein-protein network analysis for the same Trm1 AD- and PV-specific genes. Color shading of the nodes denotes AD (green)– or PV (red)–specific genes.

https://rashX.ucsf.edu), in which transcriptional abnormalities from any individual rash's Trm1 population can be placed in context of the T_H2/T_H17 AD-PV stratification shown in Fig. 6. To support a universal input format, our portal accepts standard 10X Genomics scRNA-seq immune cell dataset matrices (in an RDS file format). The web interface first identifies cells in the external dataset that are most similar to our Trm1 population. Differential gene expression analysis for the Trm1 disease–specific genes (table S7) is then performed on the external dataset's Trm1 cells in comparison to those from our HCs. Heatmaps for these AD- and PV-specific genes and a hyperdimensionality plot as in Fig. 6 are then generated for the external sample. To illustrate use of RashX, we included dataset matrices from an external AD sample and a PV sample at the website portal. Example web portal outputs showed that these samples segregated closely to their parent class (fig. S8). Thus, we have created a globally accessible resource allowing any researcher to place their disease sample scRNA-seq data in context of our Trm1 T_H2/T_H17 framework.

DISCUSSION

Here, we present single-cell transcriptomic profiles of chronic inflammatory skin disease, encompassing 24 rash and 7 HC samples. We identified 41 T cell and APC subpopulations within these samples and produced a detailed global portrait of molecular derangements unique to AD and PV. Globally, we found proliferation-driven expansion of the T_{reg} and Trm components and universal cytotoxic T cell exhaustion by diverse forms of chronic skin inflammation. Our findings indicated that T_{regs} usually proliferate in rashes in an attempt to control pathogenic skin inflammation but that one or more qualitative factors prevented successful regulation. Cytotoxic lymphocyte exhaustion was evident in every case; however, these cells harbored relatively few distinguishing abnormalities between disease classes, suggestive of a shared end state rather than a causative force.

Patient-level studies have previously attempted to identify PV- and AD-specific genetic changes, with a limited number of genes showing reproducibility between reports (*7*, *8*, *65*–*68*). We suspect that a limitation in these prior bulk profiling experiments is conflation of transcriptional differences arising in distinct cell populations. For example, both our AD and PV disease–specific transcriptional signatures were only found in $CD69^+$ $CD103^+$–resident memory T cells, which play central roles in chronic inflammatory disease. In skin disease, there is significant Trm cell infiltration of active psoriatic lesions (*60*). Underscoring their cutaneous functional importance, grafting of prepsoriatic human skin (and associated Trm cells) onto mice leads to development of psoriatic lesions, whereas blockade of cutaneous T cell migration by E-selectin inhibition does not improve PV (*69*, *70*). Trm cells are also enriched in joints and mediate arthritis flares (*71*), and expansion and/or rejunevation of $CD8^+$ pulmonary Trm cell populations after influenza infection is associated with aberrant fibrosis (*72*). The discovery of our AD- and PV-specific transcriptional signatures in Trm cells highlights the importance of this cell population in chronic tissue inflammation and identifies a large set of candidate effectors driving each disease, which can now be functionally investigated.

Transcripts distinguishing AD and PV in Trm cells included previously described T_H2- and T_H17-specific genetic abnormalities in each class [e.g., *IL17F*, *CXCL13*, *GNLY*, and *NBAS* (*9*, *37*, *48*, *49*)]. However, our data tied both known and unknown dysregulated genes into coherent signatures demonstrating recurrent patient-level segregation between the two disease classes. Each gene set also showed significantly enhanced interconnection in unbiased functional networks, indicative of biological cooperativity.

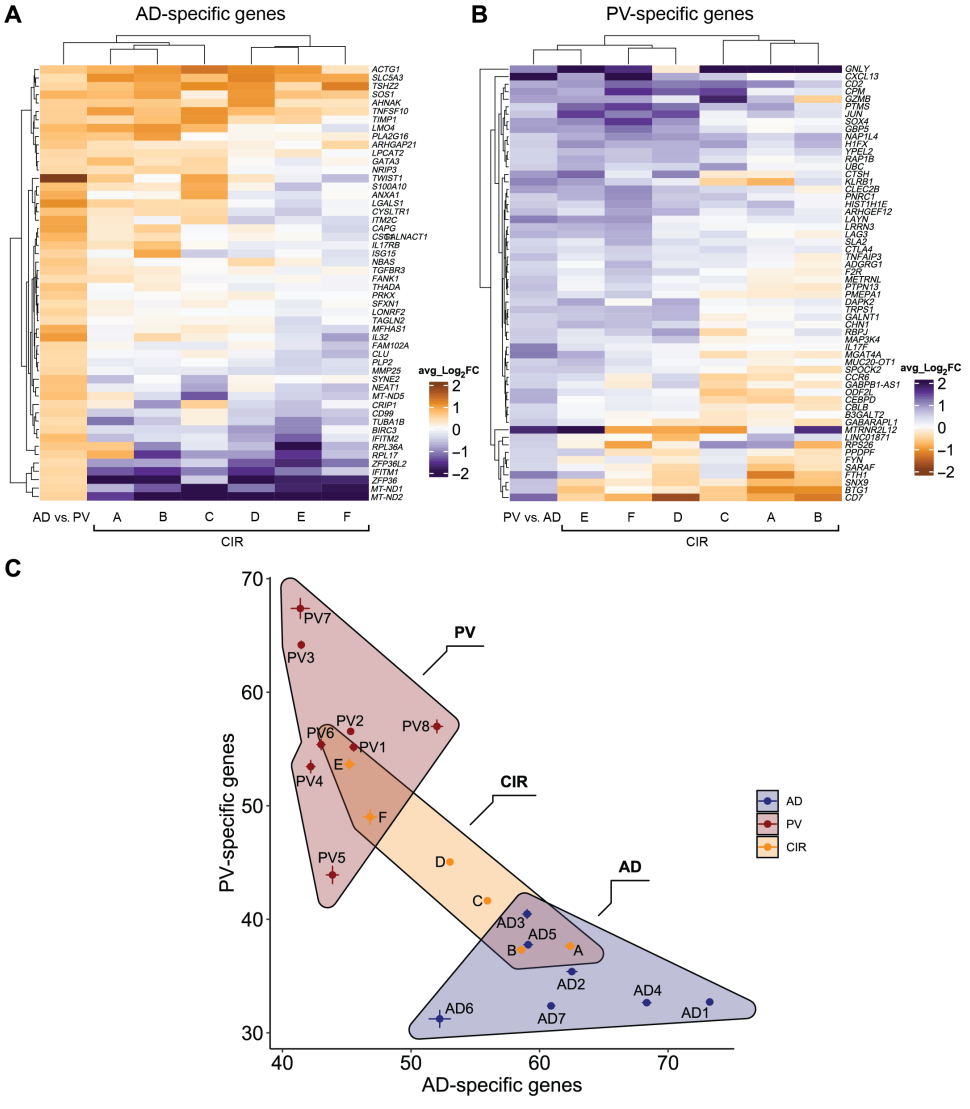

Fig. 6. CIRs show molecular stratification with AD- or PV-specific DEGs. (**A**) Heatmap showing relative expression levels (avg_log$_2$FC) for each CIR Trm1 cell population relative to Trm 1 cells from all seven HCs. Column 1 shows avg_log$_2$FC values for Trm1 cells from seven AD versus eight PV samples. Genes depicted are Trm1 AD–specific genes (table S7). (**B**) Same as (A) except genes depicted are Trm1 PV-specific genes (table S7). Column 1 shows avg_log$_2$FC values for Trm1 cells from all PV versus all AD samples. (**C**) Hyperdimensionality plot showing stratification of CIR samples relative to AD and PV samples. Each AD, PV, and CIR sample is mapped on the basis of aggregate gene score of Trm1 population AD-specific genes (*x* axis) and PV-specific genes (*y* axis). One-sided Mann-Whitney tests used to calculate significance and *P* values shown in table S8.

The PV- and AD-specific Trm1 signatures sets performed robustly, not only in classifying PV and AD samples from an unrelated, external dataset but also in discerning the T_H2/T_H17 bias of BP and LP samples. These commonalities between the BP sample and AD were consistent with the prominent type 2 inflammation of BP and its reported response to dupilumab (*73*). Similarly, LP exhibits T_H1/T_H17 activity, with reports of clinical improvement after administration of IL17 antagonists used for PV (*74*, *75*).

Our set of AD- and PV-specific Trm1 DEGs were able to match a subset of clinicopathologically ambiguous cases of skin inflammation into AD- or PV-like classes, consistent with therapeutic response to IL4Rα blockade. Although our CIRs represented only a small initial test set, these results suggest that clinical response in some fraction of such rashes may be predicted on the basis of their molecular similarity to existing diseases. Our findings thus make the case for larger, unbiased therapeutic trials based on the precision medicine approach described here.

A limitation of our study is that although comparable in size to other studies (*9*, *11*, *12*), covariates (e.g., age and anatomic location) may contribute some variability given the relatively small sample size of our dataset. Furthermore, our unbiased *CD45*$^+$ immune cell profiling strategy inevitably leads to certain populations, in particular APCs, harboring significantly fewer profiled single cells hindering discovery of their unique molecular abnormalities. Expansion of our dataset with a larger cohort of samples would both enable detection of complementary signatures in other subpopulations and further validate/generalize our T cell population discoveries. In addition, we anticipate that future samples using scRNA-seq approaches integrated with clonality assessment will allow more complex and informative analyses of inflammatory dysregulation.

Our data, in combination with published rash samples (*11*, *12*), represent the beginnings of an inflammatory skin disease resource where scRNA-seq profiles of any rash can be compared. Our web interface at https://rashX.ucsf.edu provides an immediate means to avail our data and analytic methods to the translational community in general. By placing transcriptomic features of individual rashes in the context of a large, existing dataset, we seek a standardized framework to link molecular features to disease prognosis and drug response based on contributions from clinical centers worldwide.

MATERIALS AND METHODS

Study design

We used CD45$^+$ immune cell scRNA-seq to (i) more precisely define immune cell type–specific molecular abnormalities distinguishing canonical inflammatory skin diseases (i.e., PV and classic AD) and (ii) to use these patterns to better understand individual, indeterminate cases of cutaneous inflammation displaying overlapping clinical or histopathologic features of both diseases. We assessed CD45$^+$ immune cells (~6000 cells per sample) using 10X Genomics droplet-based 3′ scRNA-seq from 31 enzymatically dissociated

skin samples (7 AD, 8 PV, 2 LP, 1 BP, 6 CIR lesional samples, and 7 healthy controls). Detailed information regarding clinical characteristics of patient samples are in table S1.

Sample collection

Written informed consent was obtained from HC and rash-affected skin donors under protocols approved by the University of California, San Francisco (UCSF) Institutional Review Board. Punch biopsies (6 mm full thickness) were obtained from lesional rash–affected skin, whereas mammoplasty and abdominoplasty surgical skin tissue discards were used for healthy control samples. Diagnoses were made by a board-certified dermatologist on the basis of clinical evaluation and histopathology of a representative hematoxylin and eosin–stained section of each skin sample reviewed by a board-certified dermatopathologist. The clinical characteristics and histopathologic diagnosis of patient samples were detailed in table S1. Samples were obtained from patients off of systemic immunosuppressives for at least 4 weeks (except for one sample) and topical steroids to the sampled area for at least 2 weeks before biopsy.

Immune cell isolation

Skin samples were initially placed in ice-cold phosphate-buffered saline (PBS) immediately after the biopsy for up to 8 hours before processing. Samples were then finely minced and transferred to 3 ml of enzymatic digestion buffer [RPMI 1640 medium, 10% heat-inactivated fetal bovine serum (FBS), collagenase type IV (200 U/ml; LS004188, Worthington), and deoxyribonuclease (200ug/ml; DN25, Sigma-Aldrich)] at 37°C for 16 to 18 hours. After overnight digestion, samples were transferred to 50-ml conical tubes, shaken vigorously for 30 s, and then filtered through a 100-μm cell strainer. Samples where CITE-seq antibodies were added before flow sorting (designated as "pre-flow" in table S10) were pelleted by centrifugation at 400*g* for 5 min and then cell surface receptors were blocked by adding 5 μl of Human TruStain FcX (BioLegend) in 100 μl of Cell Staining Buffer (BioLegend) at 4°C for 10 min. After blocking, TotalSeq-A antibodies (BioLegend, see table S10) at a concentration of 1 μg of antibody per 1 million cells and a 1:20 dilution of an anti-CD45 antibody conjugated to allophycocyanin fluorophore (Thermo Fisher Scientific) were then added for 30 min at 4°C. Cells were washed in PBS with 2% FBS, and samples were resuspended in 400 μl of Cell Staining Buffer and filtered through a 40-μm filter before adding 4′,6-diamidino-2-phenylindole (DAPI) to a final concentration of 1 μg/ml and flow sorting on an SH800 cell sorter for DAPI-negative and CD45-positive live immune cells (Sony Biotechnology). The samples were then washed one time and resuspended in Cell Staining Buffer before library preparation. Samples where CITE-seq antibodies were added subsequent to flow sorting (designated as "post-flow" in table S10) were pelleted by centrifugation at 400*g* for 5 min and then incubated with a 1:20 dilution of an anti-CD45 antibody conjugated to allophycocyanin fluorophore (Thermo Fisher Scientific) in Cell Staining Buffer (BioLegend) for 30 min at 4°C. Cells were washed in PBS with 2% FBS, and samples were resuspended in 400 μl of Cell Staining Buffer and filtered through a 40-μm filter before adding DAPI to a final concentration of 1 μg/ml and flow sorting on a SH800 cell sorter (Sony Biotechnology). After gating out cell debris and doublets, DAPI-negative and CD45-positive live immune cells were collected into 3 ml of Cell Staining Buffer. Immune cells were then spiked with 5% murine splenocytes to serve as a nonspecific background staining control for CITE-seq antibodies (see table S1 for spike-in information). Cell surface receptors were blocked by adding 5 μl of Human TruStain FcX (BioLegend) in a 100-μl reaction volume at 4°C for 10 min. After blocking, TotalSeq-A antibodies (BioLegend, see table S11) were added at a concentration of 0.5 μg per 1 million cells per antibody for 30 min at 4°C. The sample was then washed three times and resuspended in Cell Staining Buffer before library preparation.

scRNA-seq and CITE-seq library preparation and sequencing

scRNA-seq libraries profiling ~6000 cutaneous immune cells per sample were prepared by the Genomics Core Facility, UCSF Institute for Human Genetics using the Chromium Single-Cell 3′ Solution V2 or V3 kits (10X Genomics, Pleasanton, CA) per the manufacturer's protocol. For CITE-seq samples, 0.2 pmol of antibody-derived tag (ADT) additive primer was added at the RNA library cDNA amplification step. CITE-seq libraries were then prepared according to TotalSeq-A antibody manufacturer's protocol (BioLegend). In brief, 70 μl of ADT-containing cDNA amplification supernatant was purified with two rounds of 2X solid phase reversible immobilization (SPRI) beads (Beckman-Coulter) and then amplified for 14 to 20 cycles using HiFi HotStart ReadyMix (2X, KAPA, Roche Sequencing and Life Science, Wilmington, MA) and 2.5 μM oligos corresponding to SI polymerase chain reaction primer and TruSeq Small RNA PCR Primer Index-6 primers. After amplification, the resulting amplification products were purified by a 1.2X SPRI bead cleanup and then quantified with the Qubit Double-Stranded DNA High Sensitivity Assay Kit. Quality for scRNA and ADT libraries was assessed by a TapeStation D1000 ScreenTape (Agilent Technologies) and quantitated using the KAPA Library Quantitation Kit before sequencing. mRNA and ADT libraries were sequenced using an Illumina HiSeq 4000 with paired-end 150–base pair sequencing parameters. Detailed information on sequencing metrics are shown in table S9.

scRNA-seq and CITE-seq data processing

scRNA-seq and ADT FASTQ files were aligned and quantified using Cell Ranger Software (version 3.0.2, 10X Genomics) against the human GRCh38 transcriptome (v 3.0.0). For samples with mouse splenocytes spike-in, FASTQ files were aligned to a combined human and mouse genome reference GRCh38 + mm10 (v3.1.0). Empty droplets were removed as part of internal Cell Ranger quality control algorithms. Quality of cells was assessed on the basis of the total number of detected genes per cell and the percentage of mitochondrial gene counts, with removal of cells containing less than 100 or more than 6000 unique genes. Cells with percentage of reads mapped to mitochondrial genes exceeding 20% were also removed.

Doublets were detected and removed by the function scDblFinder (R package, v1.5.7) (*76*). Similar results were obtained using the DoubletFinder package (*77*). Counts were normalized using the NormalizeData function in Seurat using the scale factor (1e4) with natural log transformation. Highly variable genes (HVGs; 2000) were then selected using FindVariableFeatures() in Seurat using the "versust" method. These HVGs were then scaled and centered on the basis of individual expression values.

ADT samples with >35% antibody reads in cells were kept for downstream analysis (table S11). For ADT data, we used Seurat centered log-ratio normalization to calculate the mean and SD for a

given antibody in mouse cells (to estimate nonspecific background staining) and then used a cutoff of 1.5 × SD + mean, where the ADT density distribution for mouse and human cells was clearly separated (fig. S9 and table S10) (*17*).

Dimension reduction and unsupervised clustering

Principal components were computed using the RunPCA() function in Seurat based on HVGs. We then provided this principal components analysis matrix to the Harmony algorithm (*78*) within the Seurat workflow using sample, flow order, and mouse spike-in as technical covariates for batch correction. The batch-corrected coordinate space was then used for dimensional reduction and embedding as a UMAP representation under the RunUMAP() function in Seurat. The batch-corrected coordinate space was also used to compute the nearest neighbor graph by FindNeighbors() function (Seurat). The nearest-neighbor graph was applied to FindClusters() with the Louvain algorithm. Fourteen clusters with a resolution of 0.4 were retained on the basis of clustree results.

Cluster annotation

Cluster-specific differentially expressed genes were detected using the FindMarkers function in Seurat running MAST and was limited to genes with expression greater than 25% in either of the two populations tested, combined with a fold change cutoff of 0.25 ($\log_2$ scale). The *P* values were adjusted using the Bonferroni correction for multiple testing. Two major groups (*HLA-DRA*$^+$ myeloid cells and *CD3*$^+$ or *KLRB1*$^+$ lymphoid cells) were subclustered for additional rounds of feature detection, embedding, dimensionality reduction, visualization, and clustering under the above-described clustering workflow, with further subclustering of an indeterminate *CD3*$^+$/*KLRB1*$^+$ cluster enriched in cycling transcripts. (fig. S1C and tables S3 and S4). After removal of clusters containing a sizable proportion of nonimmune or low-quality cells, 21 *CD3*$^+$/*KLRB1*$^+$ clusters and 19 *HLA*$^-$*DR*$^+$ clusters were retained. The final 41 cluster immune cell object was composed of these subclustered populations and the original mast cell cluster and underwent supervised clustering based on 1328 high variable feature cluster markers.

Weighted Gaussian linear model for differential immune cell composition analysis

A weighted Gaussian linear model was used to analyze differential immune cell composition between rash-affected and HC samples. We denote Nik as the number of cells in a given sample (*i*) and a given cluster (*k*) and $\mathrm{Ni} = \sum k \, \mathrm{N}_i^k$ as the total number of cells in sample *i*. For each cluster *k* and sample *i*, let pi*k* = Ni*k*/Ni. We applied weighted linear models on the log cluster compositions, log(pik), with sample disease status as the predictor and the SD of log proportion, obtained using the delta method, as weights. Differential clusters were then selected with adjusted *P* value (adj_p_val) < 0.05 for the two sample *t* test for the coefficient for disease status, which characterizes the average changes of the log proportion between rash-affected and normal samples.

Differential expression analysis between rash-affected and normal skin

Differential expression analysis was performed between disease groups on a per cluster basis using the FindMarkers function from the Seurat R package using MAST (*40*) or Wilcox (Wilcoxon rank sum test) differential expression tests. For AD (or PV) versus HC DEGs, we performed a differential expression analysis with all AD (or PV) samples combined against all HC samples combined, on a per cluster basis, and then retained DEGs with adj_p_val < 0.001 and absolute average $\log_2$ fold change (abs avg_$\log_2$FC) > 0.425. For AD versus PV DEGs, we merged all statistically significant (*P* value < 0.001, |avg_$\log_2$FC| > 0.425) DEGs from the above AD versus HC and PV versus HC DEG comparisons. Using this gene list, we performed differential expression analysis between AD and PV samples. We then retained DEGs with |avg_$\log_2$FC| > 0.425 and adj_p_val < 0.001. For the 80% heterogeneity filter DEGs, we created a gene set containing significant DEGs from all combined AD (or PV) versus all combined HC sample comparisons from every cluster to perform differential expression analysis for each individual AD (or PV) sample versus all combined HCs and then retained DEGs with adj_p_val < 0.001 and abs avg_$\log_2$FC >0.425. The DEGs from the seven or eight individual AD (or PV) comparisons were then combined, and genes that were significantly expressed in at least 80% of AD (or PV) individual samples comparisons were retained. For the 80% heterogeneity filter AD versus PV comparison, we merged all statistically significant (*P* value < 0.001, |avg_$\log_2$FC| > 0.425) DEGs for the AD versus HC (80% filter) and PV versus HC (80% filter) DEG comparisons. Using this gene set, we performed differential expression analysis between all AD and PV samples. We then retained DEGs with |avg_$\log_2$FC| > 0.425 and adj_p_val < 0.001. DEG gene set scores (calculating average expression levels in a single cell minus aggregated expression of a control gene set) were generated using AddModuleScore() in the Seurat package (*79*).

Transcriptional network visualization

To map the pairwise (bivariate) single-cell transcriptional correlations between variables and the structures that emerge from these pairwise correlations, we used a method analogous to correlation network analysis (*80*). We generated a subsetted data matrix for Trm1 cluster cells (each listed in a separate row) with reads counts for AD-specific and PV-specific genes from Trm1 (|avg_$\log_2$FC| > 0.425, adj_ p_val < 0.001; each in a separate column). Then, the cor() function in the R stats packages (*81*) was used to obtain Spearman coefficients of gene-gene correlation. We then plotted an overall transcriptional network graph in the R package qgraph (version 1.3.2) (*61*) using the correlation matrix. The coordinates of each node were computed using the Fruchterman-Reingold algorithm, where the attraction between nodes is proportional to the strength of the correlation between two genes (nodes).

STRING protein interaction network visualization

AD- versus PV-specific transcripts (|avg_$\log_2$FC| > 0.425, adj_ p_val < 0.001) from Trm1 were mapped onto the STRING protein interaction network (*62*). We used the STRINGdb package in R to link the genes to proteins in the STRING database and subsetted the network to only genes corresponding to our 110 DEGs using the string_db$map object in STRINGdb. A combined score greater than 0.4 was used as a cutoff. This resulted in 108 proteins (2 genes did not map to a protein). The resulting subnetwork constrained to these 108 proteins consisted of 98 nodes with connections to other nodes. The retained interactions were visualized by igraph, where each node corresponds to a gene/protein and each edge represents existing experimental and database evidence for protein interactions.

We quantified the segregation and tested the significance between the AD-specific and PV-specific nodes on this graph by performing permutation tests conditional on the observed network. We randomly permuted the AD- or PV- specific labels for the 98 nodes (genes) and calculated the normalized cut score; we repeated this 100,000 times to construct a null distribution for the normalized cut score, conditional on this gene network. A P value was calculated as the proportion of the resampled normalized cut scores smaller than the observed normalized cut score, resulting in a P value of 0.001.

Hyperdimensionality proximity analysis

Having identified two sets of DEGs in AD and PV from Trm1 cells (table S7), we wished to visualize how samples occurred in this hyperdimensional space, summarized by these two axes. We took the aggregate gene approach described in Cao *et al.* (*82*), in which genes along one axis for any particular cell are summed over normalized gene counts with pseudocount values of 1. Because there were two gene sets of interest, we calculated these two AD and PV signatures for each cell. Cells were then grouped within sample by geometric mean. We then considered these samples bound to arbitrary regions within this hyperdimensional space and visualized these regions with hull plots using the R/ggforce (*83*) with concavity = 5. We calculated whether indeterminate (CIR), BP, LP, or external dataset AD/PV samples were more proximate to the PV or AD region by calculating the sample-wise Canberra distance matrix (*84*) across the hull plane. We then tested whether the proximity for a sample was significantly closer to PV or AD by one-sided Mann-Whitney tests for the lesser distance.

Statistical analyses

Statistical analyses were performed with RStudio v.1.4.1717 and GraphPad Prism (version 8.0; GraphPad Software, La Jolla, CA). Differential immune cell composition between two groups was analyzed with a weighted Gaussian linear model. For single-cell analysis, we used Seurat, and a generalized linear model framework that treats cellular detection rate as a covariate or a nonparametric Wilcoxon rank sum test with Bonferroni correction. The length of a segment connecting two gene signatures was measured using Euclidean distance or Canberra distance. Pearson's correlation coefficient was calculated with the R function cor(). Adjusted $P < 0.05$ is considered significant for Seurat-based analyses, whereas $P < 0.05$ was used for other analyses.

SUPPLEMENTARY MATERIALS

www.science.org/doi/10.1126/sciimmunol.abl9165
Figs. S1 to S9
Tables S1 to S11

View/request a protocol for this paper from *Bio-protocol*.

REFERENCES AND NOTES

1. T. D. Rachakonda, C. W. Schupp, A. W. Armstrong, Psoriasis prevalence among adults in the United States. *J. Am. Acad. Dermatol.* **70**, 512–516 (2014).
2. T. E. Shaw, G. P. Currie, C. W. Koudelka, E. L. Simpson, Eczema prevalence in the United States: Data from the 2003 National Survey of Children's Health. *J. Invest. Dermatol.* **131**, 67–73 (2011).
3. Z. C. Chiesa Fuxench, J. K. Block, M. Boguniewicz, J. Boyle, L. Fonacier, J. M. Gelfand, M. H. Grayson, D. J. Margolis, L. Mitchell, J. I. Silverberg, L. Schwartz, E. L. Simpson, P. Y. Ong, Atopic dermatitis in America study: A cross-sectional study examining the prevalence and disease burden of atopic dermatitis in the US adult population. *J. Invest. Dermatol.* **139**, 583–590 (2019).
4. E. L. Simpson, T. Bieber, E. Guttman-Yassky, L. A. Beck, A. Blauvelt, M. J. Cork, J. I. Silverberg, M. Deleuran, Y. Kataoka, J.-P. Lacour, K. Kingo, M. Worm, Y. Poulin, A. Wollenberg, Y. Soo, N. M. H. Graham, G. Pirozzi, B. Akinlade, H. Staudinger, V. Mastey, L. Eckert, A. Gadkari, N. Stahl, G. D. Yancopoulos, M. Ardeleanu; SOLO 1 and SOLO 2 Investigators, Two phase 3 trials of dupilumab versus placebo in atopic dermatitis. *N. Engl. J. Med.* **375**, 2335–2348 (2016).
5. S. Ferreira, E. Guttman-Yassky, T. Torres, Selective JAK1 inhibitors for the treatment of atopic dermatitis: Focus on upadacitinib and abrocitinib. *Am. J. Clin. Dermatol.* **21**, 783–798 (2020).
6. A. Menter, B. E. Strober, D. H. Kaplan, D. Kivelevitch, E. F. Prater, B. Stoff, A. W. Armstrong, C. Connor, K. M. Cordoro, D. M. R. Davis, B. E. Elewski, J. M. Gelfand, K. B. Gordon, A. B. Gottlieb, A. Kavanaugh, M. Kiselica, N. J. Korman, D. Kroshinsky, M. Lebwohl, C. L. Leonardi, J. Lichten, H. W. Lim, N. N. Mehta, A. S. Paller, S. L. Parra, A. L. Pathy, R. N. Rupani, M. Siegel, E. B. Wong, J. J. Wu, V. Hariharan, C. A. Elmets, Joint AAD-NPF guidelines of care for the management and treatment of psoriasis with biologics. *J. Am. Acad. Dermatol.* **80**, 1029–1072 (2019).
7. L. C. Tsoi, E. Rodriguez, F. Degenhardt, H. Baurecht, U. Wehkamp, N. Volks, S. Szymczak, W. R. Swindell, M. K. Sarkar, K. Raja, S. Shao, M. Patrick, Y. Gao, R. Uppala, B. E. Perez White, S. Getsios, P. W. Harms, E. Maverakis, J. T. Elder, A. Franke, J. E. Gudjonsson, S. Weidinger, Atopic dermatitis is an IL-13-dominant disease with greater molecular heterogeneity compared to psoriasis. *J. Invest. Dermatol.* **139**, 1480–1489 (2019).
8. M. Quaranta, B. Knapp, N. Garzorz, M. Mattii, V. Pullabhatla, D. Pennino, C. Andres, C. Traidl-Hoffmann, A. Cavani, F. J. Theis, J. Ring, C. B. Schmidt-Weber, S. Eyerich, K. Eyerich, Intraindividual genome expression analysis reveals a specific molecular signature of psoriasis and eczema. *Sci. Transl. Med.* **6**, 244ra90 (2014).
9. J. Liu, H.-W. Chang, Z.-M. Huang, M. Nakamura, S. Sekhon, R. Ahn, P. Munoz-Sandoval, S. Bhattarai, K. M. Beck, I. M. Sanchez, E. Yang, M. Pauli, S. T. Arron, W.-P. Fung-Leung, E. Munoz, X. Liu, T. Bhutani, J. North, A. M. Fourie, M. D. Rosenblum, W. Liao, Single-cell RNA sequencing of psoriatic skin identifies pathogenic Tc17 cell subsets and reveals distinctions between $CD8^+$ T cells in autoimmunity and cancer. *J. Allergy Clin. Immunol.* **147**, 2370–2380 (2021).
10. J. B. Cheng, A. J. Sedgewick, A. I. Finnegan, P. Harirchian, J. Lee, S. Kwon, M. S. Fassett, J. Golovato, M. Gray, R. Ghadially, W. Liao, B. E. Perez White, T. M. Mauro, T. Mully, E. A. Kim, H. Sbitany, I. M. Neuhaus, R. C. Grekin, S. S. Yu, J. W. Gray, E. Purdom, R. Paus, C. J. Vaske, S. C. Benz, J. S. Song, R. J. Cho, Transcriptional programming of normal and inflamed human epidermis at single-cell resolution. *Cell Rep.* **25**, 871–883 (2018).
11. C. Bangert, K. Rindler, T. Krausgruber, N. Alkon, F. M. Thaler, H. Kurz, T. Ayub, D. Demirtas, N. Fortelny, V. Vorstandlechner, W. M. Bauer, T. Quint, M. Mildner, C. Jonak, A. Elbe-Bürger, J. Griss, C. Bock, P. M. Brunner, Persistence of mature dendritic cells, T_H2A, and Tc2 cells characterize clinically resolved atopic dermatitis under IL-4Rα blockade. *Sci. Immunol.* **6**, abe2749 (2021).
12. G. Reynolds, P. Vegh, J. Fletcher, E. F. M. Poyner, E. Stephenson, I. Goh, R. A. Botting, N. Huang, B. Olabi, A. Dubois, D. Dixon, K. Green, D. Maunder, J. Engelbert, M. Efremova, K. Polański, L. Jardine, C. Jones, T. Ness, D. Horsfall, J. McGrath, C. Carey, D.-M. Popescu, S. Webb, X. Wang, B. Sayer, J.-E. Park, V. A. Negri, D. Belokhvostova, M. D. Lynch, D. McDonald, A. Filby, T. Hagai, K. B. Meyer, A. Husain, J. Coxhead, R. Vento-Tormo, S. Behjati, S. Lisgo, A.-C. Villani, J. Bacardit, P. H. Jones, E. A. O'Toole, G. S. Ogg, N. Rajan, N. J. Reynolds, S. A. Teichmann, F. M. Watt, M. Haniffa, Developmental cell programs are co-opted in inflammatory skin disease. *Science* **371**, aba6500 (2021).
13. Y. Liu, C. Cook, A. J. Sedgewick, S. Zhang, M. S. Fassett, R. R. Ricardo-Gonzalez, P. Harirchian, S. W. Kashem, S. Hanakawa, J. R. Leistico, J. P. North, M. A. Taylor, W. Zhang, M.-Q. Man, A. Charruyer, N. Beliakova-Bethell, S. C. Benz, R. Ghadially, T. M. Mauro, D. H. Kaplan, K. Kabashima, J. Choi, J. S. Song, R. J. Cho, J. B. Cheng, Single-cell profiling reveals divergent, globally patterned immune responses in murine skin inflammation. *iScience* **23**, 101582 (2020).
14. H. He, H. Suryawanshi, P. Morozov, J. Gay-Mimbrera, E. Del Duca, H. J. Kim, N. Kameyama, Y. Estrada, E. Der, J. G. Krueger, J. Ruano, T. Tuschl, E. Guttman-Yassky, Single-cell transcriptome analysis of human skin identifies novel fibroblast subpopulation and enrichment of immune subsets in atopic dermatitis. *J. Allergy Clin. Immunol.* **145**, 1615–1628 (2020).
15. T. B. Rojahn, V. Vorstandlechner, T. Krausgruber, W. M. Bauer, N. Alkon, C. Bangert, F. M. Thaler, F. Sadeghyar, N. Fortelny, V. Gernedl, K. Rindler, A. Elbe-Bürger, C. Bock, M. Mildner, P. M. Brunner, Single-cell transcriptomics combined with interstitial fluid proteomics defines cell type-specific immune regulation in atopic dermatitis. *J. Allergy Clin. Immunol.* **146**, 1056–1069 (2020).
16. R. Salomon, D. Kaczorowski, F. Valdes-Mora, R. E. Nordon, A. Neild, N. Farbehi, N. Bartonicek, D. Gallego-Ortega, Droplet-based single cell RNAseq tools: A practical guide. *Lab Chip* **19**, 1706–1727 (2019).
17. M. Stoeckius, C. Hafemeister, W. Stephenson, B. Houck-Loomis, P. K. Chattopadhyay, H. Swerdlow, R. Satija, P. Smibert, Simultaneous epitope and transcriptome measurement in single cells. *Nat. Methods* **14**, 865–868 (2017).

18. T. Stuart, A. Butler, P. Hoffman, C. Hafemeister, E. Papalexi, W. M. Mauck III, Y. Hao, M. Stoeckius, P. Smibert, R. Satija, Comprehensive integration of single-cell data. *Cell* **177**, 1888–1902.e21 (2019).
19. L. Zappia, A. Oshlack, Clustering trees: A visualization for evaluating clusterings at multiple resolutions. *Gigascience* **7**, giy083 (2018).
20. H. Choi, H. Song, Y. W. Jung, The roles of CCR7 for the homing of memory CD8+ T cells into their survival niches. *Immune Netw.* **20**, e20 (2020).
21. R. Watanabe, A. Gehad, C. Yang, L. L. Scott, J. E. Teague, C. Schlapbach, C. P. Elco, V. Huang, T. R. Matos, T. S. Kupper, R. A. Clark, Human skin is protected by four functionally and phenotypically discrete populations of resident and recirculating memory T cells. *Sci. Transl. Med.* **7**, 279ra39 (2015).
22. M. Willemsen, R. Linkutė, R. M. Luiten, T. R. Matos, Skin-resident memory T cells as a potential new therapeutic target in vitiligo and melanoma. *Pigment Cell Melanoma Res.* **32**, 612–622 (2019).
23. P. A. Szabo, H. M. Levitin, M. Miron, M. E. Snyder, T. Senda, J. Yuan, Y. L. Cheng, E. C. Bush, P. Dogra, P. Thapa, D. L. Farber, P. A. Sims, Single-cell transcriptomics of human T cells reveals tissue and activation signatures in health and disease. *Nat. Commun.* **10**, 4706 (2019).
24. G. Mijnheer, L. Lutter, M. Mokry, M. van der Wal, R. Scholman, V. Fleskens, A. Pandit, W. Tao, M. Wekking, S. Vervoort, C. Roberts, A. Petrelli, J. G. C. Peeters, M. Knijff, S. de Roock, S. Vastert, L. S. Taams, J. van Loosdregt, F. van Wijk, Conserved human effector Treg cell transcriptomic and epigenetic signature in arthritic joint inflammation. *Nat. Commun.* **12**, 2710 (2021).
25. M. Vaeth, Y.-H. Wang, M. Eckstein, J. Yang, G. J. Silverman, R. S. Lacruz, K. Kannan, S. Feske, Tissue resident and follicular Treg cell differentiation is regulated by CRAC channels. *Nat. Commun.* **10**, 1183 (2019).
26. F. Boix-Giner, O. Millan, D. San Segundo, P. Muñoz-Cacho, E. Mancebo, S. Llorente, L. Rafael-Valdivia, A. Rimola, E. Fábrega, A. Mrowiec, L. Allende, A. Minguela, J. M. Bolarín, E. Paz-Artal, M. López-Hoyos, M. Brunet, M. Muro, High frequency of central memory regulatory T cells allows detection of liver recipients at risk of early acute rejection within the first month after transplantation. *Int. Immunol.* **28**, 55–64 (2016).
27. L. K. Ward-Kavanagh, W. W. Lin, J. R. Šedý, C. F. Ware, The TNF receptor superfamily in co-stimulating and co-inhibitory responses. *Immunity* **44**, 1005–1019 (2016).
28. E. Y. Chiang, P. E. de Almeida, D. E. de Almeida Nagata, K. H. Bowles, X. Du, A. S. Chitre, K. L. Banta, Y. Kwon, B. McKenzie, S. Mittman, R. Cubas, K. R. Anderson, S. Warming, J. L. Grogan, CD96 functions as a co-stimulatory receptor to enhance $CD8^+$ T cell activation and effector responses. *Eur. J. Immunol.* **50**, 891–902 (2020).
29. L. T. Nguyen, P. S. Ohashi, Clinical blockade of PD1 and LAG3 — potential mechanisms of action. *Nat. Rev. Immunol.* **15**, 45–56 (2015).
30. S. Li, H. Morita, M. Sokolowska, G. Tan, T. Boonpiyathad, L. Opitz, K. Orimo, S. K. Archer, K. Jansen, M. L. K. Tang, D. Purcell, M. Plebanski, C. A. Akdis, Gene expression signatures of circulating human type 1, 2, and 3 innate lymphoid cells. *J. Allergy Clin. Immunol.* **143**, 2321–2325 (2019).
31. G. Rizzo, E. Vafadarnejad, P. Arampatzi, J.-S. Silvestre, A. Zernecke, A.-E. Saliba, C. Cochain, Single-cell transcriptomic profiling maps monocyte/macrophage transitions after myocardial infarction in mice. *bioRxiv*, 2020.04.14.040451 (2020). https://doi.org/10.1101/2020.04.14.040451.
32. C. Cochain, E. Vafadarnejad, P. Arampatzi, J. Pelisek, H. Winkels, K. Ley, D. Wolf, A.-E. Saliba, A. Zernecke, Single-cell RNA-seq reveals the transcriptional landscape and heterogeneity of aortic macrophages in murine atherosclerosis. *Circ. Res.* **122**, 1661–1674 (2018).
33. L. Zhang, Z. Li, K. M. Skrzypczynska, Q. Fang, W. Zhang, S. A. O'Brien, Y. He, L. Wang, Q. Zhang, A. Kim, R. Gao, J. Orf, T. Wang, D. Sawant, J. Kang, D. Bhatt, D. Lu, C.-M. Li, A. S. Rapaport, K. Perez, Y. Ye, S. Wang, X. Hu, X. Ren, W. Ouyang, Z. Shen, J. G. Egen, Z. Zhang, X. Yu, Single-cell analyses inform mechanisms of myeloid-targeted therapies in colon cancer. *Cell* **181**, 442–459.e29 (2020).
34. M. Stoeckius, C. Hafemeister, W. Stephenson, B. Houck-Loomis, P. K. Chattopadhyay, H. Swerdlow, R. Satija, P. Smibert, Large-scale simultaneous measurement of epitopes and transcriptomes in single cells. *Nat. Methods* **14**, 865–868 (2017).
35. Q. Zhang, Y. He, N. Luo, S. J. Patel, Y. Han, R. Gao, M. Modak, S. Carotta, C. Haslinger, D. Kind, G. W. Peet, G. Zhong, S. Lu, W. Zhu, Y. Mao, M. Xiao, M. Bergmann, X. Hu, S. P. Kerkar, A. B. Vogt, S. Pflanz, K. Liu, J. Peng, X. Ren, Z. Zhang, Landscape and dynamics of single immune cells in hepatocellular carcinoma. *Cell* **179**, 829–845.e20 (2019).
36. J. Chen, Y. Tan, F. Sun, L. Hou, C. Zhang, T. Ge, H. Yu, C. Wu, Y. Zhu, L. Duan, L. Wu, N. Song, L. Zhang, W. Zhang, D. Wang, C. Chen, C. Wu, G. Jiang, P. Zhang, Single-cell transcriptome and antigen-immunoglobin analysis reveals the diversity of B cells in non-small cell lung cancer. *Genome Biol.* **21**, 152 (2020).
37. J. Jiang, A. Faiz, M. Berg, O. A. Carpaij, C. J. Vermeulen, S. Brouwer, L. Hesse, S. A. Teichmann, N. H. T. ten Hacken, W. Timens, M. van den Berge, M. C. Nawijn, Gene signatures from scRNA-seq accurately quantify mast cells in biopsies in asthma. *Clin. Exp. Allergy* **50**, 1428–1431 (2020).
38. R. E. Scott, P. N. Ghule, J. L. Stein, G. S. Stein, Cell cycle gene expression networks discovered using systems biology: Significance in carcinogenesis. *J. Cell. Physiol.* **230**, 2533–2542 (2015).
39. R. Takahashi, Y. Kano, Y. Yamazaki, M. Kimishima, Y. Mizukawa, T. Shiohara, Defective regulatory T cells in patients with severe drug eruptions: Timing of the dysfunction is associated with the pathological phenotype and outcome. *J. Immunol.* **182**, 8071–8079 (2009).
40. G. Finak, A. McDavid, M. Yajima, J. Deng, V. Gersuk, A. K. Shalek, C. K. Slichter, H. W. Miller, M. J. McElrath, M. Prlic, P. S. Linsley, R. Gottardo, MAST: A flexible statistical framework for assessing transcriptional changes and characterizing heterogeneity in single-cell RNA sequencing data. *Genome Biol.* **16**, 278 (2015).
41. E. Ermis, S. K. Celik, N. Solak, G. C. Genc, A. Dursun, The role of GNLY gene polymorphisms in psoriasis pathogenesis. *An. Bras. Dermatol.* **94**, 198–203 (2019).
42. H. G. Dursun, H. O. Yılmaz, R. Dursun, S. Kulaksızoğlu, Association of cytotoxic T lymphocyte antigen-4 gene polymorphisms with psoriasis vulgaris: A case-control study in turkish population. *J. Immunol. Res.* **2018**, 1–10 (2018).
43. A. S. Haider, M. A. Lowes, H. Gardner, R. Bandaru, K. Darabi, F. Chamian, T. Kikuchi, P. Gilleaudeau, M. S. Whalen, I. Cardinale, I. Novitskaya, J. G. Krueger, Novel insight into the agonistic mechanism of alefacept in vivo: Differentially expressed genes may serve as biomarkers of response in psoriasis patients. *J. Immunol.* **178**, 7442–7449 (2007).
44. R. H. Fiechter, H. M. de Jong, L. J. J. van Mens, I. A. Fluri, S. W. Tas, D. L. P. Baeten, N. G. Yeremenko, M. G. H. van de Sande, IL-12p40/IL-23p40 blockade with ustekinumab decreases the synovial inflammatory infiltrate through modulation of multiple signaling pathways including MAPK-ERK and Wnt. *Front. Immunol.* **12**, 611656 (2021).
45. C. J. Nunes-Santos, G. Uzel, S. D. Rosenzweig, PI3K pathway defects leading to immunodeficiency and immune dysregulation. *J. Allergy Clin. Immunol.* **143**, 1676–1687 (2019).
46. U. Niesner, I. Albrecht, M. Janke, C. Doebis, C. Loddenkemper, M. H. Lexberg, K. Eulenburg, S. Kreher, J. Koeck, R. Baumgrass, K. Bonhagen, T. Kamradt, P. Enghard, J. Y. Humrich, S. Rutz, U. Schulze-Topphoff, O. Aktas, S. Bartfeld, H. Radbruch, A. N. Hegazy, M. Löhning, D. C. Baumgart, R. Duchmann, M. Rudwaleit, T. Häupl, I. Gitelman, V. Krenn, J. Gruen, J. Sieper, M. Zeitz, B. Wiedenmann, F. Zipp, A. Hamann, M. Janitz, A. Scheffold, G. R. Burmester, H. D. Chang, A. Radbruch, Autoregulation of Th1-mediated inflammation by *twist1*. *J. Exp. Med.* **205**, 1889–1901 (2008).
47. G. Seumois, J. Zapardiel-Gonzalo, B. White, D. Singh, V. Schulten, M. Dillon, D. Hinz, D. H. Broide, A. Sette, B. Peters, P. Vijayanand, Transcriptional profiling of Th2 cells identifies pathogenic features associated with asthma. *J. Immunol.* **197**, 655–664 (2016).
48. K. W. Kim, R. A. Myers, J. H. Lee, C. Igartua, K. E. Lee, Y. H. Kim, E.-J. Kim, D. Yoon, J.-S. Lee, T. Hirota, M. Tamari, A. Takahashi, M. Kubo, J.-M. Choi, K.-E. Kim, D. L. Nicolae, C. Ober, M. H. Sohn, Genome-wide association study of recalcitrant atopic dermatitis in Korean children. *J. Allergy Clin. Immunol.* **136**, 678–684.e4 (2015).
49. S. Arriba-Mendez, C. Sanz, M. Isidoro-Garcia, I. Davild, E. Laffond, E. Horeno, C. Avila, F. Lorente, 927T>C polymorphism of the cysteinyl-leukotriene type-1 receptor (CYSLTR1) gene in children with asthma and atopic dermatitis. *Pediatr. Allergy Immunol.* **17**, 323–328 (2006).
50. M. Yamashita, K. Hirahara, R. Shinnakasu, H. Hosokawa, S. Norikane, M. Y. Kimura, A. Hasegawa, T. Nakayama, Crucial role of MLL for the maintenance of memory T helper type 2 cell responses. *Immunity* **24**, 611–622 (2006).
51. C. A. Tibbitt, J. M. Stark, L. Martens, J. Ma, J. E. Mold, K. Deswarte, G. Oliynyk, X. Feng, B. N. Lambrecht, P. De Bleser, S. Nylén, H. Hammad, M. Arsenian Henriksson, Y. Saeys, J. M. Coquet, Single-cell RNA sequencing of the T helper cell response to house dust mites defines a distinct gene expression signature in airway Th2 cells. *Immunity* **51**, 169–184.e5 (2019).
52. D. A. Rafei-Shamsabadi, C. S. N. Klose, T. Y. F. Halim, Y. Tanriver, T. Jakob, Context dependent role of type 2 innate lymphoid cells in allergic skin inflammation. *Front. Immunol.* **10**, 2591 (2019).
53. M. Vocanson, A. Hennino, A. Rozières, G. Poyet, J.-F. Nicolas, Effector and regulatory mechanisms in allergic contact dermatitis. *Allergy* **64**, 1699–1714 (2009).
54. D. Hijnen, E. F. Knol, Y. Y. Gent, B. Giovannone, S. Beijn, T. S. Kupper, C. A. F. M. Bruijnzeel-Koomen, R. A. Clark, $CD8^+$ T cells in the lesional skin of atopic dermatitis and psoriasis patients are an important source of IFN-γ, IL-13, IL-17 and IL-22. *J. Invest. Dermatol.* **133**, 10.1038/jid.2012.456 (2013).
55. M. Suárez-Fariñas, S. Tintle, A. Shemer, A. Chiricozzi, K. Nograles, I. Cardinale, S. Duan, A. Bowcock, J. G. Krueger, E. Guttman-Yassky, Non-lesional atopic dermatitis (AD) skin is characterized by broad terminal differentiation defects and variable immune abnormalities. *J. Allergy Clin. Immunol.* **127**, 954–964.e1–4 (2011).
56. S. Bruhn, Y. Fang, F. Barrenäs, M. Gustafsson, H. Zhang, A. Konstantinell, A. Krönke, B. Sönnichsen, A. Bresnick, N. Dulyaninova, H. Wang, Y. Zhao, J. Klingelhöfer, N. Ambartsumian, M. K. Beck, C. Nestor, E. Bona, Z. Xiang, M. Benson, A generally applicable translational strategy identifies S100A4 as a candidate gene in allergy. *Sci. Transl. Med.* **6**, 218ra4 (2014).
57. N. Bhagavathula, K. C. Nerusu, G. J. Fisher, G. Liu, A. B. Thakur, L. Gemmell, S. Kumar, Z. H. Xu, P. Hinton, N. Tsurushita, N. F. Landolfi, J. J. Voorhees, J. Varani, Amphiregulin and epidermal hyperplasia: Amphiregulin is required to maintain the psoriatic phenotype of human skin grafts on severe combined immunodeficient mice. *Am. J. Pathol.* **166**, 1009–1016 (2005).

58. Y. Pan, T. S. Kupper, Metabolic reprogramming and longevity of tissue-resident memory T cells. *Front. Immunol.* **9**, 1347 (2018).
59. R. A. Clark, Skin-resident T cells: The ups and downs of on site immunity. *J. Investig. Dermatol.* **130**, 362–370 (2010).
60. S. Cheuk, M. Wikén, L. Blomqvist, S. Nylén, T. Talme, M. Ståhle, L. Eidsmo, Epidermal Th22 and Tc17 cells form a localized disease memory in clinically healed psoriasis. *J. Immunol.* **192**, 3111–3120 (2014).
61. S. Epskamp, A. O. J. Cramer, L. J. Waldorp, V. D. Schmittmann, D. Borsboom, qgraph: Network visualizations of relationships in psychometric data. *J. Stat. Softw.* **48**, 1–18 (2012).
62. D. Szklarczyk, A. L. Gable, D. Lyon, A. Junge, S. Wyder, J. Huerta-Cepas, M. Simonovic, N. T. Doncheva, J. H. Morris, P. Bork, L. J. Jensen, C. von Mering, STRING v11: Protein–protein association networks with increased coverage, supporting functional discovery in genome-wide experimental datasets. *Nucleic Acids Res.* **47**, D607–D613 (2019).
63. J. Shi, J. Malik, Normalized cuts and image segmentation. *IEEE Trans. Pattern Anal. Mach. Intell.* **22**, 888–905 (2000).
64. J. N. Cohen, S. Bowman, Z. G. Laszik, J. P. North, Clinicopathologic overlap of psoriasis, eczema, and psoriasiform dermatoses: A retrospective study of T helper type 2 and 17 subsets, interleukin 36, and β-defensin 2 in spongiotic psoriasiform dermatitis, sebopsoriasis, and tumor necrosis factor α inhibitor-associated dermatitis. *J. Am. Acad. Dermatol.* **82**, 430–439 (2020).
65. A. Rawat, D. Rinchai, M. Toufiq, A. K. Marr, T. Kino, M. Garand, Z. Tatari-Calderone, B. S. A. Kabeer, N. Krishnamoorthy, D. Bedognetti, M. Y. Karim, K. S. Sastry, D. Chaussabel, A neutrophil-driven inflammatory signature characterizes the blood transcriptome fingerprint of psoriasis. *Front. Immunol.* **11**, 587946 (2020).
66. M. Keermann, S. Kõks, E. Reimann, E. Prans, K. Abram, K. Kingo, Transcriptional landscape of psoriasis identifies the involvement of IL36 and IL36RN. *BMC Genomics* **16**, 322 (2015).
67. B. Li, L. C. Tsoi, W. R. Swindell, J. E. Gudjonsson, T. Tejasvi, A. Johnston, J. Ding, P. E. Stuart, X. Xing, J. J. Kochkodan, J. J. Voorhees, H. M. Kang, R. P. Nair, G. R. Abecasis, J. T. Elder, Transcriptome analysis of psoriasis in a large case-control sample: RNA-seq provides insights into disease mechanisms. *J. Invest. Dermatol.* **134**, 1828–1838 (2014).
68. H. He, R. Bissonnette, J. Wu, A. Diaz, E. Saint-Cyr Proulx, C. Maari, C. Jack, M. Louis, Y. Estrada, J. G. Krueger, N. Zhang, A. B. Pavel, E. Guttman-Yassky, Tape strips detect distinct immune and barrier profiles in atopic dermatitis and psoriasis. *J. Allergy Clin. Immunol.* **147**, 199–212 (2020).
69. M. Bhushan, T. O. Bleiker, A. E. Ballsdon, M. H. Allen, M. Sopwith, M. K. Robinson, C. Clarke, R. P. J. B. Weller, R. A. C. Graham-Brown, M. Keefe, J. N. W. N. Barker, C. E. M. Griffiths, Anti-E-selectin is ineffective in the treatment of psoriasis: A randomized trial. *Br. J. Dermatol.* **146**, 824–831 (2002).
70. O. Boyman, H. P. Hefti, C. Conrad, B. J. Nickoloff, M. Suter, F. O. Nestle, Spontaneous development of psoriasis in a new animal model shows an essential role for resident T cells and tumor necrosis factor-α. *J. Exp. Med.* **199**, 731–736 (2004).
71. M. H. Chang, A. Levescot, N. Nelson-Maney, R. B. Blaustein, K. D. Winden, A. Morris, A. Wactor, S. Balu, R. Grieshaber-Bouyer, K. Wei, L. A. Henderson, Y. Iwakura, R. A. Clark, D. A. Rao, R. C. Fuhlbrigge, P. A. Nigrovic, Arthritis flares mediated by tissue-resident memory T cells in the joint. *Cell Rep.* **37**, 109902 (2021).
72. Z. Wang, S. Wang, N. P. Goplen, C. Li, I. S. Cheon, Q. Dai, S. Huang, J. Shan, C. Ma, Z. Ye, M. Xiang, A. H. Limper, E.-C. Porquera, J. E. Kohlmeier, M. H. Kaplan, N. Zhang, A. J. Johnson, R. Vassallo, J. Sun, PD-1^{hi} CD8^{+} resident memory T cells balance immunity and fibrotic sequelae. *Sci. Immunol.* **4**, eaaw1217 (2019).
73. R. Abdat, R. A. Waldman, V. de Bedout, A. Czernik, M. Mcleod, B. King, S. Gordon, R. Ahmed, A. Nichols, M. Rothe, D. Rosmarin, Dupilumab as a novel therapy for bullous pemphigoid: A multicenter case series. *J. Am. Acad. Dermatol.* **83**, 46–52 (2020).
74. T. Schmidt, F. Solimani, R. Pollmann, R. Stein, A. Schmidt, I. Stulberg, K. Kühn, R. Eming, V. Eubel, P. Kind, N. Arweiler, C. Sitaru, M. Hertl, T_H1/T_H17 cell recognition of desmoglein 3 and bullous pemphigoid antigen 180 in patients with lichen planus. *J. Allergy Clin. Immunol.* **142**, 669–672.e7 (2018).
75. F. Solimani, R. Pollmann, T. Schmidt, A. Schmidt, X. Zheng, R. Savai, S. Mühlenbein, J. Pickert, V. Eubel, C. Möbs, R. Eming, M. Hertl, Therapeutic targeting of Th17/Tc17 cells leads to clinical improvement of lichen planus. *Front. Immunol.* **10**, 1808 (2019).
76. P.-L. Germain, A. Lun, *scDblFinder: scDblFinder* (Bioconductor version: release 3.13, 2021); https://bioconductor.org/packages/scDblFinder/.
77. C. S. McGinnis, L. M. Murrow, Z. J. Gartner, DoubletFinder: Doublet detection in single-cell RNA sequencing data using artificial nearest neighbors. *Cell Syst.* **8**, 329–337.e4 (2019).
78. I. Korsunsky, N. Millard, J. Fan, K. Slowikowski, F. Zhang, K. Wei, Y. Baglaenko, M. Brenner, P.-R. Loh, S. Raychaudhuri, Fast, sensitive and accurate integration of single-cell data with Harmony. *Nat. Methods* **16**, 1289–1296 (2019).
79. I. Tirosh, B. Izar, S. M. Prakadan, M. H. Wadsworth II, D. Treacy, J. J. Trombetta, A. Rotem, C. Rodman, C. Lian, G. Murphy, M. Fallahi-Sichani, K. Dutton-Regester, J.-R. Lin, O. Cohen, P. Shah, D. Lu, A. S. Genshaft, T. K. Hughes, C. G. K. Ziegler, S. W. Kazer, A. Gaillard, K. E. Kolb, A.-C. Villani, C. M. Johannessen, A. Y. Andreev, E. M. Van Allen, M. Bertagnolli, P. K. Sorger, R. J. Sullivan, K. T. Flaherty, D. T. Frederick, J. Jané-Valbuena, C. H. Yoon, O. Rozenblatt-Rosen, A. K. Shalek, A. Regev, L. A. Garraway, Dissecting the multicellular ecosystem of metastatic melanoma by single-cell RNA-seq. *Science* **352**, 189–196 (2016).
80. P. Langfelder, S. Horvath, Fast R functions for robust correlations and hierarchical clustering. *J. Stat. Softw.* **46**, i11 (2012).
81. R: The R Project for Statistical Computing; https://r-project.org/.
82. J. Cao, M. Spielmann, X. Qiu, X. Huang, D. M. Ibrahim, A. J. Hill, F. Zhang, S. Mundlos, L. Christiansen, F. J. Steemers, C. Trapnell, J. Shendure, The single-cell transcriptional landscape of mammalian organogenesis. *Nature* **566**, 496–502 (2019).
83. Accelerating ggplot2; https://ggforce.data-imaginist.com/.
84. P. Dixon, VEGAN, a package of R functions for community ecology. *J. Veg. Sci.* **14**, 927–930 (2003).

Acknowledgments: We wish to thank R. Sevey for assistance with figure illustration and S. Mukhopadhyay for RashX website development. **Funding:** This project was supported in part by grants from the National Institute of Arthritis and Musculoskeletal and Skin Diseases of the National Institutes of Health K08AR067243 to J.B.C., the LEO foundation to R.J.C., NIH NIAMS R01AR061106 to T.M.M. (administered by the Northern California Institute for Research and Education), NIH NIAMS K08AR075880 to R.R.R.-G., and NIH/NCRR UCSF-CTSI grant number UL1TR001872. J.B.C. is a recipient of research awards from the National Eczema Association and National Psoriasis Foundation. This study was supported in part by funds from Sun Pharmaceutical Industries and Sanofi. Its contents are solely the responsibility of the authors and do not necessarily represent the official views of the National Institutes of Health or the Department of Veterans Affairs. **Author contributions:** Y.L., J.B.C., and R.J.C. designed the study. E.K., R.G., R.C.G., J.B.C., and R.J.C. supervised sample collection and processing. Y.L., C.C., and P.H. performed sample preparation and analysis. Y.L., H.W., M.T., C.C., A.M.-B., and E.P. performed computational analysis. J.P.N. performed histopathology analysis. Y.L., H.W., E.P., J.B.C., and R.J.C. wrote the original manuscript with contributions from C.C., J.P.N., P.H., A.A.H., Z.Z., R.G., R.R.R.-G., R.C.G., T.M.M., E.K., and J.C. **Competing interests:** J.B.C. and R.J.C. are investigators for Sun Pharmaceutical Industries, LEO Pharmaceuticals, and Sanofi (grants to their institution). All other authors declare that they have no competing interests. **Data and materials availability:** Sequencing BAM files are deposited at the European Genome-Phenome Archive (EGA), which is hosted by the EBI and the CRG under accession number EGAS00001005271. The processed Seurat objects with cell identities are available at Zenodo (https://zenodo.org/deposit/5228495). All statistical analysis and plotting of scRNA-seq and cell surface protein data were performed using RStudio software (version 1.4.1717). All analysis scripts are available at the online repository (https://github.com/Yale73/scRNA-seq-for-diverse-human-rashes). The online rash mapping web-based interface is available at https://rashX.ucsf.edu. Further information and requests for resources and reagents should be directed to and will be fulfilled by the lead contacts J.B.C. (Jeffrey.Cheng@ucsf.edu) or R.J.C. (Raymond.cho@ucsf.edu).

Submitted 26 August 2021
Accepted 11 March 2022
Published 15 April 2022
10.1126/sciimmunol.abl9165

Science Immunology

Classification of human chronic inflammatory skin disease based on single-cell immune profiling

Yale Liu, Hao Wang, Mark Taylor, Christopher Cook, Alejandra Martnez-Berdeja, Jeffrey P. North, Paymann Harirchian, Ashley A. Hailer, Zijun Zhao, Ruby Ghadially, Roberto R. Ricardo-Gonzalez, Roy C. Grekin, Theodora M. Mauro, Esther Kim, Jaehyuk Choi, Elizabeth Purdom, Raymond J. Cho, and Jeffrey B. Cheng

Sci. Immunol., **7** (70), eabl9165.
DOI: 10.1126/sciimmunol.abl9165

Gene interface tool to identify your rash

Many chronic skin conditions are caused by imbalances in the immune milieu of the environment, yet many of these changes remain under characterized. Here, Liu and Wang *et al.* used single-cell profiling of immune cells from skin samples of atopic dermatitis (AD), psoriasis vulgaris (PV), and healthy controls to profile the immune signatures of the different diseases. They found that AD and PV samples had distinct T cell resident memory, innate lymphoid cell, and CD8+ T cell gene signatures that could be validated in an external dataset. Using these signatures, they created a tool that could classify previously clinicopathologically indeterminate rash samples. This tool is now available as a web resource (RashX) for anyone to use to help further classify skin rashes.

Science Immunology (ISSN) is published by the American Association for the Advancement of Science. 1200 New York Avenue NW, Washington, DC 20005. The title *Science Immunology* is a registered trademark of AAAS.